

SIMULATING ATMOSPHERIC DISPERSION WITHIN THE CITY EINDHOVEN

A thesis submitted to the Delft University of Technology in partial fulfillment
of the requirements for the degree of

Master of Science in Environmental Engineering of Civil Engineering and Geosciences

by

Hannah Herbschleb

September 2021

Supervisors: Dr. Stephan de Roode (TU Delft)
Dr. Ir. Ruud Janssen (TNO)
Prof. Dr. Pier Siebesma (TU Delft)
Prof. Dr. Ir. Herman Russchenberg (TU Delft)

The work in this thesis was made in association with:

TNO innovation
for life

Climate, Air and Sustainability
TNO

TU Delft Delft
University of
Technology

Faculty of Civil Engineering and Geosciences
Delft University of Technology

Hannah Herbschleb: *Simulating atmospheric dispersion within the city Eindhoven* (2021)
Student number: 4312589

Abstract

The Dutch Atmospheric Large Eddy Simulation (DALES) model is used to investigate the addition of an urban area to DALES and its impact on the dispersion of a pollutant in non-neutral boundary conditions. Two different states of the boundary layer are investigated, a stable boundary layer (SBL) and a convective boundary layer (CBL), which are primarily achieved by a prescribed time-dependent surface flux, negative for a SBL and positive for a CBL.

A module is added to DALES to provide the addition of heterogeneous emission sources. Several emission sources are implemented, one line source and three point sources which locations depend on their location in the city. All sources emit from the surface level. For the applied urban area, a part of Eindhoven is selected, containing several relatively high buildings, a high way and a measurement cite. Unfortunately, the results from these simulations could not be validated with the measurements due to several model constraints.

The dispersion of a pollutant within a stable and a convective boundary layer is first compared without buildings to the Gaussian plume model, to analyze and attempt to verify the dispersion results obtained from DALES. The concentrations of the pollutant in a SBL as calculated by DALES and the Gaussian plume model are remarkably similar. The largest differences in concentration are at the source and very close to the source, which is difficult to calculate for both models. The differences between the CBL of DALES and the Gaussian plume model are more significant, as the concentrations calculated by DALES are a factor 10 smaller than obtained from the Gaussian plume model. The difference in concentration levels between DALES' SBL and CBL is almost a factor 20, demonstrating the importance of turbulence on the dispersion.

The presence of an urban area influences the concentration of a pollutant severely, regardless the stability of the atmosphere. The effect is larger in stable night-time conditions, than convective day-time conditions. Due to the presence of buildings, the concentrations of the pollutant is more concentrated at and around the source, while at larger distances the concentration decrease with respect to simulations without buildings. In a stable boundary layer, the surface concentrations up to a downwind distance of 200m from the source are larger with the presence of buildings than without. In a convective boundary layer, the downwind distance from which the surface concentration increases due to the presence of buildings is considerably smaller: 50m, due to the larger turbulences present in the CBL. These results could be highly dependent on the wind velocity, placing of buildings and the source, vertical domain size, the lack of moisture, and turbulence. These factors require further investigation to advance the study of the implementation of an urban area in DALES.

Contents

1	INTRODUCTION	3
1.1	Modeling the atmosphere	3
1.2	Objectives and outline	4
2	DALES	7
2.1	Background	7
2.2	Prognostic variables	8
2.3	Governing Equations	8
2.4	Turbulent Kinetic Energy	9
2.4.1	Subfilter-scale TKE	9
2.4.2	TKE Budget Equation	10
2.5	Boundary Conditions	11
2.5.1	Surface flux model	11
2.5.2	Immersed Boundary Method	12
2.5.3	Boundary conditions: lateral domain	14
2.6	Advection	14
2.7	Addition of heterogeneous emission sources	15
3	GAUSSIAN PLUME MODEL	17
3.1	Point source model	17
3.2	Line source model	18
3.2.1	Dispersion equations	18
4	SET-UP OF THE SIMULATIONS	21
4.1	Simulation time and domain size	21
4.2	Subsidence and inversion jump	22
4.3	Surface temperature flux	23
4.4	Initial geostrophic wind velocity and advection scheme	24
4.5	Subgrid Turbulent Kinetic Energy	25
4.6	Surface boundary condition: implemented elevation map	25
4.7	Source locations	26
4.8	Differences between the GABLS1 and this study's SBL	27
5	ANALYSIS OF ATMOSPHERIC CONDITIONS	29
5.1	Establishing the simulations	29
5.1.1	Stable Boundary Layer (SBL)	29
5.1.2	Convective Boundary Layer (CBL)	30
5.2	Effect of the addition of obstacles	32
5.2.1	Expectations	32
5.2.2	SBL results	33
5.2.3	CBL results	34
6	DISPERSION ANALYSIS	35
6.1	Comparison with the Gaussian plume model	35
6.1.1	Surface concentrations	37
6.1.2	Vertical profiles	39
6.1.3	Development over time	40
6.1.4	Conclusion	40
6.2	Comparison with the urban area	41
6.2.1	Surface concentrations	43
6.2.2	Vertical profiles	43
6.2.3	Development over time	45
6.2.4	Conclusion	45
6.3	Influence of a different advection scheme	46

6.3.1	Development over time	48
6.3.2	Conclusion	49
7	CONCLUSIONS AND RECOMMENDATIONS	51
7.1	Conclusions	51
7.1.1	Effect of the addition of obstacles	51
7.1.2	Dispersion	52
7.2	Recommendations	53
A	INPUTFILES FOR THE DALES SIMULATIONS	59
A.1	Settings - namoptions	59
A.2	Vertical profiles - prof.inp	61
A.3	Large scale forcings - lscale.inp	61
A.4	Large scale fluxes - ls_flux.inp	61
A.5	Additional inputfiles	61
B	TRANSITION OF GABLS1 TO SBL	63
C	RESULTS OF THE POINT SOURCES	67

List of Figures

Figure 1.1	Measured surface concentrations of NO_x and PM_{10}	5
Figure 2.1	Immersed Boundary Method: schematic overview	13
Figure 2.2	Example of the input file for the immersed boundary method	13
Figure 2.3	Boundary conditions: default DALES and new	14
Figure 2.4	Schematic overview of nudging boundaries	15
Figure 2.5	Example of the input file for source locations	16
Figure 2.6	Example of the emission rates for source locations	16
Figure 4.1	Course of the modeled potential temperature	23
Figure 4.2	Vertical profile of the potential liquid temperature of the SBL and CBL simulations	24
Figure 4.3	Initial vertical profile of the initial Subgrid-TKE values for SBL and CBL simulations	25
Figure 4.4	Locations of the measuring sites in Eindhoven and the simulated area	26
Figure 4.5	Elevation map of Eindhoven: original and cleaned	26
Figure 4.6	The locations of the scalars in the IBM domain.	27
Figure 5.1	Comparison of the GABLS1 simulations versus this study's SBL simulation	30
Figure 5.2	Vertical profiles of the CBL simulation of the buoyancy flux, TKE, vertical velocity variance and the TKE budget.	31
Figure 5.3	Surface concentrations of the SBL simulation with obstacles	32
Figure 5.4	Impact of the obstacles on the stable boundary layer, expressed with vertical profiles of several variables	33
Figure 5.5	Impact of the obstacles on the convective boundary layer, expressed with vertical profiles of several variables	34
Figure 6.1	Visualisation of the pollutant concentration of the DALES and Gaussian plume SBL simulations.	36
Figure 6.2	Visualisation of the pollutant concentration of the DALES and Gaussian plume CBL simulations.	37
Figure 6.3	Concentrations of the line sources in the downwind direction	38
Figure 6.4	Differences in simulated concentrations between SBL and CBL	38
Figure 6.5	Informative figure of the sources and analyzed downwind distances from the source	39
Figure 6.6	Vertical profiles of the concentration from the DALES and Gaussian plume model at several downwind distances from the line source	40
Figure 6.7	Development of the concentration over time of DALES without IBM and the Gaussian plume model	41
Figure 6.8	Vertical and horizontal profiles of time-averaged concentrations of DALES with obstacles and without	42
Figure 6.9	Comparison with and without obstacles of concentrations of the line sources in the downwind direction	43
Figure 6.10	Vertical profiles of the concentrations within the SBL and CBL, with and without IBM at several downwind distances from the source	44
Figure 6.11	Vertical distribution in percentages of concentrations of SBL and CBL, with and without IBM	45
Figure 6.12	Development of the surface concentration over time of DALES of both the stable and convective boundary layer	45

Figure 6.13	Vertical and horizontal profiles of time-averaged concentrations of the Kappa advection scheme, in comparison to 2nd order and Gaussian plume	47
Figure 6.14	Surface concentrations of different advection schemes	48
Figure 6.15	Vertical profile distribution of concentrations of the two different advection schemes	48
Figure 6.16	Development of surface concentrations over time of the simulation with the Kappa advection scheme	49
Figure B.1	Vertical profiles of the total buoyancy flux of the GABLS simulation in comparison to small alterations to the desired simulation state	64
Figure B.2	Vertical profiles of the total TKE and the SFS-TKE of the GABLS simulation in comparison to small alterations to the desired simulation state	65
Figure B.3	Vertical profiles of the ratio between the total TKE and the SFS-TKE of the GABLS simulation in comparison to small alterations to the desired simulation state	65
Figure C.1	Vertical and horizontal profiles of time-averaged concentrations of the SBL as calculated by the Gaussian plume model and DALES with obstacles and without	68
Figure C.2	Vertical and horizontal profiles of time-averaged concentrations of the CBL as calculated by the Gaussian plume model and DALES with obstacles and without	69
Figure C.3	Concentrations of the point sources in the downwind direction	70
Figure C.4	Vertical profiles of the concentration from the DALES and Gaussian plume model at several downwind distances from the point source	70

1

Introduction

The presence of industries providing our way of life has severely impacted the earth in the past 100 years, resulting in the current climate crisis. One of the most important aspects of the climate crisis is the state of the atmosphere, specifically air pollution and the dispersion hereof. The increasing air pollution in urban areas, which are inhabited by the majority of the world population, is a growing problem [WHO, 2016]. To gain insight into the current situation and estimate the impact of possible changes to the urban layout or emission patterns, atmospheric models are required to accurately simulate the lower part of the atmosphere (the Atmospheric Boundary Layer) on a scale smaller than 10 meters between two grid points.

The atmospheric boundary layer is the part of the atmosphere influenced by the surface, and follows a diurnal cycle. During the day, the atmospheric boundary layer depth increases and typically grows to several kilometers. The sun warms the Earth's surface causing convection. The resulting turbulence increases the mixing layer height, which is the level at which the atmospheric boundary layer meets the free atmosphere. This turbulence impacts the dispersion strength of particles, especially the vertical dispersion. During the night, the cooling of the ground surfaces causes a strong reduction of turbulence, resulting in a lower, stable boundary layer which typically reaches around the 200m. The remaining turbulence is mainly caused by the wind shear in the horizontal direction. In a boundary layer without obstacles like buildings, the direction and the strength of the dispersion is mostly dictated by the wind direction and turbulence. The addition of an urban area will influence this dispersion strength.

1.1 Modeling the atmosphere

Many studies simulating the atmosphere are based upon computational fluid dynamics (CFD). There are several different implementations of CFD. In 2019, Yang et al. proposed a model to investigate the influences between urban form, urban air pollution, and the wind environment using a Reynolds-averaged Navier-Stokes model (RANS). This method is based on statistical averaging of turbulence, and assumes the turbulent diffusion to be proportional to the fields' mean concentration. This leads to relatively fast and steady, two-dimensional equations.

Another widely used type of CFD is Large-Eddy Simulation (LES), which is based on resolving turbulence using local filtering. It is able to resolve turbulent scales with a filter width¹ between 1 and 50 meters [Heus et al., 2010]. LES can resolve up to 90% of all turbulence. This method can calculate the turbulence in 3D, and therefore, it is more time-expensive than RANS.

Fortunately, multiple comparisons between RANS with LES with respect to the dispersion of pollutants in urban areas have been performed [Jia and Kikumoto, 2021; Yang et al., 2019; Tominaga et al., 2008]. All concluded that LES is more accurate in terms of concentration's strength and location. Therefore, this study will not take a RANS model into account. The LES model this study uses is the fourth version of the Dutch Atmospheric Large-Eddy Simulation model (DALES₄). A more in-depth description of DALES is given in chapter 2.

Several studies have investigated the processes and physics in LES models of urban areas. Walton and Cheng modeled an urban area in steady-state, neutral conditions, where the implemented LES model lacked the complexity provided by DALES in terms of the governing turbulence equations. Others have investigated flow and dispersion in urban areas with the LES model PALM (Parallelized Large-Eddy Simulation Model), taking a stable atmosphere and radiation into account. However, these versions of the PALM model have a 2D urban model and energy balance solvers [Letzel et al., 2008; Xie et al., 2008, 2013; Resler et al., 2017], whereas Grylls et al. is currently working on a more complex version of simulating an urban area in DALES₄, uDALES. This version was not available for this study, and a previous version of this model is applied which is an model based on the findings of ? implemented by [Koene, 2020].

Verzijlbergh et al. [2009] has investigated the dispersion of pollutants within DALES, comparing cloudy and non-cloudy conditions. However, the dispersion in urban areas in non-neutral conditions is not yet investigated. The objective of this study is to simulate the dispersion of a pollutant in an convective and stable boundary layer, with and without structures, to investigate the capabilities of DALES to simulate an urban area. The main research question is:

What is the influence of obstacles on the dispersion of a pollutant within Eindhoven, in stable and convective boundary layers?

This study will not take any form of moisture into account, for example clouds or precipitation. The only varying aspects of the simulations are the addition of the obstacles and the stability of the atmosphere; all other variables are constant when differentiating between simulations.

1.2 Objectives and outline

The selected area is the Dutch city Eindhoven, which has had problems with air pollutions due to its highway through the city, the nearby airport, and the city's agriculture [Ascenso et al., 2021]. The Dutch National Institute for Public Health and the Environment (RIVM) has been measuring the particulate matter (PM) and the NO_x concentrations across the country for several years, including certain locations within Eindhoven. The topology implemented in the DALES simulations will be based on one of these locations. Figure 1.1 gives the hourly surface concentrations of days with clear-sky conditions, measured at one of these sites in Eindhoven.

¹ The filter width is a function of the grid size

Ideally, the results obtained from the DALES simulations are compared against the measurements, to statistically determine the accuracy of the simulations. This study is a small step in that direction.

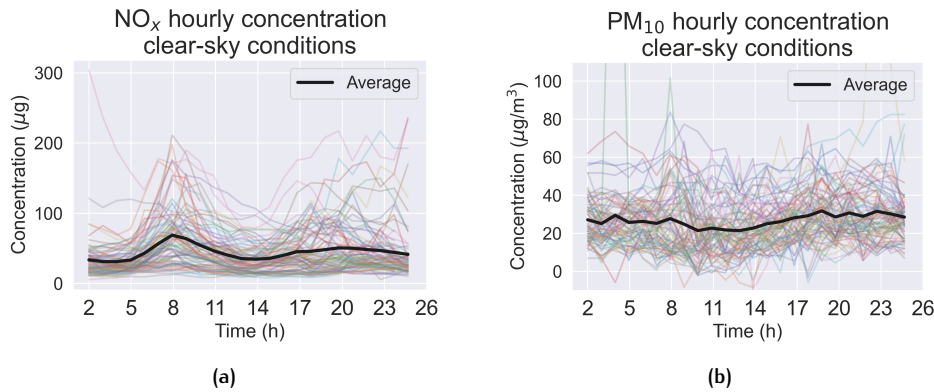


Figure 1.1: Measured surface concentrations of NO_x and PM₁₀ of all days meeting the requirements, and the hourly average.

The approach of this study is to first validate the simulated stable and convective boundary layer with the help of a widely used dispersion model, the Gaussian plume model, and investigate the effect of the added urban area by comparing the results from the DALES simulations with and without buildings.

First, chapter 2 elaborates on the current version of DALES and the additions made for this study, followed by an explanation of the Gaussian plume model in chapter 3. Chapter 4 gives insight into the set-up of all simulations by elaborating on the different prescribed variables and settings. The results are divided in two chapters, first the atmospheric conditions are analyzed to establish a proper simulation of both the stable and convective boundary layer in chapter 5. The dispersion of all simulations is analyzed in chapter 6, starting with the stable boundary layer, with and without obstacles, followed by the results of the convective boundary layer, and finishing with a comparison between the two. The conclusions and recommendations are given in chapter 7.

2

DALES

First, this chapter will give insight into the background of DALES, the prognostic variables, and the governing equations it uses, in respectively section 2.1, 2.2 and 2.3. This is followed by the turbulence kinetic energy (TKE) calculations in section 2.4, and an explanation of the boundary conditions of DALES, the immersed boundary layer and the lateral domain in section 2.5. Finally, section 2.6 gives the implemented advection scheme and section 2.7 describes the additional model for the implementation of multiple sources at different locations.

2.1 Background

Results of DALES simulations were first published in 1986 and is based on the pioneering LES modeling principles of Lilly [1967], Deardorff [1974], Sommeria [1976], and Nieuwstadt and Brost [1986]. Especially the latter forms the base of the current LES-codes of DALES, written in the language Fortran95. Since, DALES has had many contributors, which resulted in the current version, DALES4, which is maintained and further developed by researchers of the Technical University of Delft, the Royal Netherlands Meteorology Institute (KNMI), the University of Wageningen, and the Max Planck Institute for Meteorology [Heus et al., 2010].

DALES consists of a multitude of modules that perform specific parts of the calculations. All the modules are called upon when needed from the main module, which can be run on command. This clear set-up enables the user to easily add or modify a module. The simulations require several input files which contain the initial and boundary conditions of the simulated environment and the required settings for the simulation. While all the input files and most of the output is ASCII files, the larger datasets are stored in Network Common Data Form (NetCDF) version 3 or higher.

2.2 Prognostic variables

DALES takes several time-dependent prognostic variables as input which determine the course of the simulations. These variables are the three velocity components u_i in $x, y,$ and z direction, the total water specific humidity q_t , rain water specific humidity q_r , the liquid potential temperature θ_l , rain droplet number concentration N_r and a maximum of 100 passive or active scalar ϕ . The wind in x -direction is specified from west to east and in the y -direction from south to north [Heus et al., 2010]. The total water specific humidity is defined as:

$$q_t = q_v + q_c, \quad (2.1)$$

where the total water specific humidity is equal to the sum of the water vapor specific humidity q_v and the cloud liquid water specific humidity q_c . Given that there will not be any moisture present in any of the simulations, the values of q_v and q_c are:

$$q_v = 0, \quad (2.2)$$

$$q_c = 0 \quad (2.3)$$

making the value of the total water specific humidity equal to zero ($q_t = 0$).

The liquid water potential temperature and the liquid water virtual potential temperature are calculated with the following equations:

$$\theta_l \approx \theta - \frac{L}{c_{pd}\Pi} q_c \quad (2.4)$$

$$\theta_v \approx \left(\theta - \frac{L}{c_{pd}\Pi} q_c \right) \left(1 - \left(1 - \frac{R_v}{R_d} \right) q_t - \frac{R_v}{R_d} q_c \right) \quad (2.5)$$

where θ , which is a function of the temperature $T = \theta\Pi$, is the potential temperature, L and c_{pd} are constants of the latent and specific heat respectively and Π is a function of the pressure (the Exner function). R_d and R_v are respectively the gas constants for dry air and water vapor, with $R_d = 287.0 \text{ Jkg}^{-1}\text{K}^{-1}$ and $R_v = 461.5 \text{ Jkg}^{-1}\text{K}^{-1}$. Due to the lack of moisture (with $q_t = q_v = q_c = 0$) equation 2.5 results in $\theta_v \approx \theta_l \approx \theta$.

2.3 Governing Equations

DALES core equations are based on the Navier-Stokes equations with the Boussinesq approximation with a reference state (ρ_0, p_0, θ_0) . The equations of motion are given by the continuity equation (2.6), the Boussinesq approximation of the Navier-Stokes equation (2.7), and the filtered transport equation for scalars (2.8).

$$\frac{\partial \tilde{u}_i}{\partial x_i} = 0, \quad (2.6)$$

$$\frac{\partial \tilde{u}_i}{\partial t} = -\frac{\partial \tilde{u}_i \tilde{u}_j}{\partial x_j} - \frac{\partial \pi}{\partial x_i} + \frac{g}{\theta_0} \tilde{\theta}_v \delta_{i3} + \mathcal{F}_i - \frac{\partial \tau_{ij}}{\partial x_j}, \quad (2.7)$$

$$\frac{\partial \tilde{\phi}}{\partial t} = -\frac{\partial \tilde{u}_i \tilde{\phi}}{\partial x_j} - \frac{\partial R_{u_j, \phi}}{\partial x_j} + S_\phi \quad (2.8)$$

The tildes represent the filtered mean variables, \mathcal{F}_i the large scale forcings, and with the modified pressure $\pi = \frac{\tilde{p}}{\phi_0} + \frac{2}{3}e$ with \tilde{p} the filtered pressure, ρ_0 the reference state density and e the subfilter-scale turbulence kinetic energy (SFS-TKE). τ_{ij} represents

$\widetilde{u_i u_j} - \widetilde{u_i} \widetilde{u_j} - \frac{2}{3}e$, which is part of the subgrid momentum flux, which is parameterized. π is computed with a Poisson equation of $\frac{\partial^2 \pi}{\partial x_i^2}$, where the divergence $\frac{\partial}{\partial x_i}$ is taken of equation 2.7. Combined with the continuity equation 2.6, the left-hand side of equation 2.7, $\frac{\partial \widetilde{u_i}}{\partial t}$ is equal to zero. This results in the following equation:

$$\frac{\partial^2 \pi}{\partial x_i^2} = \frac{\partial}{\partial x_i} \left(-\frac{\partial \widetilde{u_i} \widetilde{u_j}}{\partial x_j} + \frac{g}{\theta_0} \widetilde{\theta_v} \delta_{i3} + \mathcal{F}_i - \frac{\partial \tau_{ij}}{\partial x_j} \right). \quad (2.9)$$

With π and τ_{ij} , DALES can calculate the resolved and subgrid fluxes due to eddies, which is elaborated in section 2.4.

Similarly, in the transport equation for scalars φ , the $R_{u_j \varphi}$ represents the SFS scalar fluxes by $\widetilde{u_j \varphi} - \widetilde{u_j} \widetilde{\varphi}$. S_φ denotes the source terms of the scalar.

2.4 Turbulent Kinetic Energy

The turbulent kinetic energy (TKE) is a useful parameter to analyze the turbulence in a boundary layer. The total TKE consists of the resolved TKE and the subfilter-scale turbulent kinetic energy (SFS-TKE). All simulations must be designed in terms of required mesh size and resolution, such that the total TKE is not dominated by the SFS-TKE, and most is resolved.

The resolved TKE is best analyzed with the help of the TKE budget equation. Section 2.4.2 gives an explanation of the equations and implementations. The calculations of the subfilter-scale TKE are key closure equations of DALES, where the turbulent kinetic energy a of a scale smaller than the filter width are parameterized, which is elaborated below.

2.4.1 Subfilter-scale TKE

The SFS fluxes in DALES are parameterized with the help of a downgradient eddy diffusivity approach:

$$R_{u_j \varphi} = -K_h \frac{\partial \widetilde{\varphi}}{\partial x_j}, \quad (2.10)$$

$$\tau_{ij} = -K_m \left(\frac{\partial \widetilde{u_i}}{\partial x_j} + \frac{\partial \widetilde{u_j}}{\partial x_i} \right) \quad (2.11)$$

where K_h and K_m are the eddy viscosity and diffusivity coefficients. These can be modeled in DALES by two methods: as a function of SFS-TKE e proposed by Deardorff [1974] or the Smagorinsky closure [Smagorinsky, 1963]. This study will only focus on the SFS-TKE model of Deardorff, where $\frac{\partial e}{\partial t}$ is a function of $R_{u_j \varphi}$ and τ_{ij} :

$$\frac{\partial e}{\partial t} = -\frac{\partial \widetilde{u_j e}}{\partial x_j} - \tau_{ij} \frac{\partial \widetilde{u_i}}{\partial x_j} + \frac{g}{\theta_0} R_{w, \theta_v} - \frac{\partial R_{u_j e}}{\partial x_j} - \frac{1}{\rho_0} \frac{\partial R_{u_j \pi}}{\partial x_j} - \varepsilon \quad (2.12)$$

where ε represents the SFS-TKE dissipation rate. The first and the second terms on the right-hand-side are resp. solved and calculated with equation 2.11. The third term represents the buoyancy SFS-TKE production, which is calculated with

$$\frac{g}{\theta_0} R_{w, \theta_v} = \frac{g}{\theta_0} (A R_{w, \theta_t} + B R_{w, \theta_t}) \quad (2.13)$$

where A and B are dependent on a dry or moist local thermodynamic state. As stated before, only a dry atmosphere will be simulated in this study, resulting in the following equations for A and B :

$$A = 1 + \frac{R_v}{R_d} \tilde{q}_t \quad (2.14)$$

$$B = \left(\frac{R_v}{R_d} - 1 \right) \theta_0 \quad (2.15)$$

where θ_0 is the reference potential temperature. The remaining terms of equation 2.12 are together parameterized with:

$$-\frac{\partial}{\partial x_j} \left(R_{u_j, e} + \frac{1}{\rho_0} R_{u_j, \pi} \right) = \frac{\partial}{\partial x_j} \left(2K_m \frac{\partial e}{\partial x_j} \right) \quad (2.16)$$

K_h and K_m are parameterized after Deardorff [1980] as shown in the equations below. These equations take several constants, which are given in table 2.1.

$$K_m = c_m \lambda e^{1/2} \quad (2.17)$$

$$K_h = c_h \lambda e^{1/2} \quad (2.18)$$

with

$$c_m = \frac{c_f}{2\pi} \left(\frac{3}{2} \alpha \right)^{-\frac{3}{2}} \quad (2.19)$$

$$c_h = \left(1 + 2 \frac{\lambda}{\Delta} \right) c_m \quad (2.20)$$

and λ depending on the grid size $\Delta = (\Delta x \cdot \Delta y \cdot \Delta z)^{1/3}$, and the stability of the flow $N = \left(\frac{g}{\theta_0} \frac{\partial \tilde{\theta}_v}{\partial z} \right)^2$:

$$\lambda = \min \left(\Delta, c_N \frac{e^{1/2}}{N} \right). \quad (2.21)$$

α	c_m	c_f	c_N
1.5	0.12	2.5	0.76

Table 2.1: Constants in equations 2.17 - 2.21

In the case of a very stable boundary layer, $\lambda \ll \Delta$, resulting in $\frac{K_h}{K_m} \approx 1$ and in the case of neutral or convective conditions, $\frac{K_h}{K_m} = 3$.

2.4.2 TKE Budget Equation

The turbulent kinetic energy budget E gives insight into the contribution of which turbulence term to the total kinetic energy. This can be calculated by applying Reynolds decomposition to the Boussinesq approximation of the Navier-Stokes equation (2.7). The total tendency of the TKE is then given by:

$$\begin{aligned} \left\langle \frac{\partial E}{\partial t} \right\rangle &\equiv \left\langle \frac{\partial}{\partial t} \left[\frac{1}{2} \left(\tilde{u}''^2 + \tilde{v}''^2 + \tilde{w}''^2 \right) \right] \right\rangle \\ &= - \underbrace{\left[\langle \tilde{u}'' \tilde{w}'' \rangle \frac{\partial \langle \tilde{u} \rangle}{\partial z} + \langle \tilde{v}'' \tilde{w}'' \rangle \frac{\partial \langle \tilde{v} \rangle}{\partial z} \right]}_{\text{shear production}} + \underbrace{\frac{g}{\tilde{\theta}_0} \langle \tilde{w} \tilde{\theta}_v \rangle}_{\text{buoyancy production}} \\ &\quad - \underbrace{\frac{\partial \langle \tilde{w}'' E \rangle}{\partial z}}_{\text{turbulent transport}} - \underbrace{\frac{\partial \langle \tilde{w}'' \pi'' \rangle}{\partial z}}_{\text{pressure correlation}} - \underbrace{\langle \varepsilon \tau \rangle}_{\text{viscous dissipation}} \end{aligned} \quad (2.22)$$

Here, the double prime " denotes the deviation from the slab-average indicated by $\langle \rangle$, and the dissipation term is given by:

$$\varepsilon_\tau = \tilde{u}_j'' \frac{\partial}{\partial x_j} \left(K_m \left[\frac{\partial \tilde{u}_i''}{\partial x_j} + \frac{\partial \tilde{u}_j''}{\partial x_i} \right] \right) \quad (2.23)$$

where K_m is the eddy diffusivity. All these different terms are evaluated at different positions due to DALES' staggered grid, requiring interpolations. Therefore the TKE budget is not entirely closed, leaving a residual. Fortunately, the implemented budget equations and interpolation techniques are well-defined, and therefore the residual is insignificant.

2.5 Boundary Conditions

2.5.1 Surface flux model

To enable the exchange between scalars at the surface and the atmosphere, and to parameterize the turbulent drag, DALES requires a surface model. The surface fluxes here are denoted by $F_{s,\phi} = \overline{w\phi} - \tilde{w}\tilde{\phi}$ of arbitrary variable ϕ . This differs from the previously defined value R , since the fluctuations in the vertical velocity at the surface are zero. As given in Heus et al. [2010], this model is based on the following equations:

$$F_{s,u} = -C_M \langle U_1 \rangle \tilde{u}_1 \quad (2.24)$$

$$F_{s,v} = -C_M \langle U_1 \rangle \tilde{v}_1 \quad (2.25)$$

$$F_{s,\phi} = -C_\phi \langle U_1 \rangle (\tilde{\phi}_1 - \phi_0) \quad (2.26)$$

where equations 2.24 and 2.24 calculate the momentum fluxes along the horizontal wind vectors, and equation 2.26 the scalar flux. C_M and C_ϕ are the drag coefficients, which are calculated with

$$C_M = \frac{u_{*0}^2}{\langle U_1 \rangle^2} \quad (2.27)$$

$$C_\phi = \frac{u_{*0}^2 \phi_{*0}}{\langle U_1 \rangle \langle \tilde{\phi}_1 - \phi_0 \rangle}. \quad (2.28)$$

All variables with $\langle \phi_i \rangle$ represent the horizontally averaged gradient at the model level i , $\langle U_1 \rangle = \sqrt{\langle \tilde{u}_1 \rangle^2 + \langle \tilde{v}_1 \rangle^2}$, u_{*0} is the averaged friction velocity and ϕ_{*0} the scalar scales. u_{*0} is unknown beforehand and therefore the Monin-Obukhov similarity theory is applied. This relates the bulk Richardson number (Ri_B), which can be calculated with equation 2.30, to the Obukhov length (L) of the lowest layer of the atmosphere between the surface to $z1$. The values of u_{*0} and ϕ_{*0} can be calculated with the help of these parameterizations. The applied equations are:

$$Ri_B = \frac{z_1}{L} \frac{\left[\ln \left(\frac{z_1}{z_{0h}} \right) - \psi_H \left(\frac{z_1}{L} \right) + \psi_H \left(\frac{z_{0h}}{L} \right) \right]}{\left[\ln \left(\frac{z_1}{z_{0m}} \right) - \psi_M \left(\frac{z_1}{L} \right) + \psi_M \left(\frac{z_{0m}}{L} \right) \right]^2} \quad (2.29)$$

$$Ri_B = \frac{g}{\theta_0} \frac{z_1 \left(\langle \widetilde{\theta_{v1}} \rangle - \langle \widetilde{\theta_{v0}} \rangle \right)}{\langle U_1 \rangle^2} \quad (2.30)$$

$$L = - \frac{u_{*0}^3}{\kappa \frac{g}{\langle \theta_{v0} \rangle} \langle F_{s,\theta_v} \rangle} \quad (2.31)$$

$$\varphi_{*0} = - \frac{\langle F_{s,\phi} \rangle}{u_{*0}} \quad (2.32)$$

where z_{0m} and z_{0h} denote the roughness length from momentum and heat, ψ_M and ψ_H are integrated stability functions. $\langle \widetilde{\theta_{v0}} \rangle$ and $\langle \widetilde{\theta_{v1}} \rangle$ are the spatially averaged filtered virtual potential temperature of the surface level and the first level of the model, respectively and κ is the Von Karman coefficient.

There are four different options for this surface model in DALES, differentiating in complexity and required input, where the surface scalar fluxes, scalar values, and u_{*0} are prescribed or parameterized as described above, or with a Land Surface Model as input. The possibility to add obstacles to the model (the Immersed Boundary Method) is currently only implemented for a surface model where the surface scalar and momentum fluxes are parameterized and the scalar fluxes at the surface can be prescribed (in DALES option 2).

2.5.2 Immersed Boundary Method

The Immersed Boundary Method is a technique that models the surface boundary conditions in fluid dynamics simulations with obstacles. This method was first implemented in DALES by [Tomas et al. \[2016\]](#) and is further developed by a TU Delft Masters Graduate [Koene \[2020\]](#).

Methodology

Every time step, the Immersed Boundary Method first calculates the flow without any obstacles, subsequently changing the flow properties at the wall. First, the modeled velocities perpendicular to the wall of the object, in the adjacent grid cell $u_{i,j,k}$, are changed to zero, by imposing a counterforce that forces the momentum tendencies to zero, which is called direct forcing. On flows parallel to the wall, the presence of a wall has a shear effect.

Consider a grid point with its cell center at location (i, j, k) , adjacent to an obstacle in the direction of the flow (here u), as shown in figure 2.1.

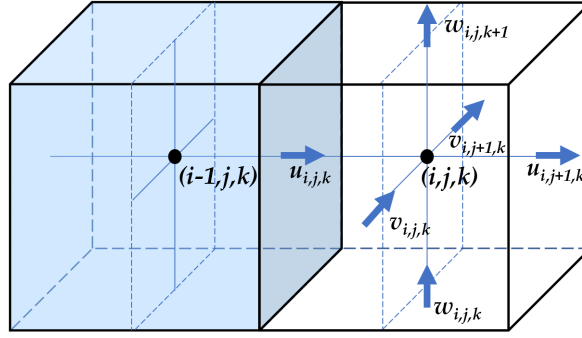


Figure 2.1: A schematic overview of two adjacent grid cells, with an obstacle present at location $(i - 1, j, k)$, and flow in u -direction. Modeled after a figure from Koene [2020]

The velocities parallel to the wall, v and w , experience shear stress. Here, the turbulent diffusions between the two cells, which would have been modeled without an obstacle, are replaced with the wall shear stress. It is applied to both $v_{i,j,k}$ and $v_{i,j+1,k}$ at the edges of the grid cell, and similarly to $w_{i,j,k}$ and $w_{i,j,k+1}$. The shear stress is calculated with

$$|\tau| = \rho \left[\frac{1-B}{2} A^{\frac{1+B}{1-B}} \left(\frac{v}{\Delta x_i} \right)^{1+B} + \frac{1+B}{A} \left(\frac{v}{\Delta x_i} \right)^B |u_{tan}| \right]^{\frac{2}{1+B}} \quad (2.33)$$

with

$$|u_{tan}| = \frac{v}{2\Delta x_i} A^{\frac{2}{1-B}} \quad (2.34)$$

where $A = 8.3$, $B = \frac{1}{7}$ and the kinematic viscosity ν is denoted with that of air, which equals $1.41 \times 10^{-5} \text{ m}^2\text{s}^{-1}$.

Implementation

To implement the height of the obstacles, DALES requires an input file containing a 2D matrix with the grid size of the surface ($i_{tot} \times j_{tot}$). This matrix contains the elevation from the surface of every grid point. It is programmed such that DALES sees these elevations as the top of the building, and vertically models every underlying grid point as an obstacle. This elevation is scaled to fit the vertical resolution. Figure 2.2 gives an example of an input-file for an immersed boundary layer with two square objects. With an $\Delta z = 5\text{m}$, the upper left object translates to a building with a height of 5m, and the lower right 10m. The IBM currently implemented in DALES models stationary, impermeable obstacles.

```

1 1 0 0 0
1 1 0 0 0
0 0 0 0 0
0 0 2 2 0
0 0 2 2 0

```

Figure 2.2: An example of the input file for the implemented objects with the immersed boundary method.

2.5.3 Boundary conditions: lateral domain

The boundary conditions of the sides and top of the domain in DALES are implemented as periodic boundary conditions; what leaves one side of the domain, reappears on the opposite side. This is illustrated in 2D in figure 2.3a. Periodic boundary layers are undesirable in this study, due to the fact that a concentration could then be present or even accumulating in behind the source, considering the direction of the flow. Therefore, a small piece of code is added to DALES following a method of Dorp [2016], where an additional nudging variable is implemented which smoothly nudges the tendencies of the scalars to zero, from a variable distance from the boundaries, defined as the nudging depth d_{nudge} . Figure 2.3b gives a schematic overview of a nudged domain.

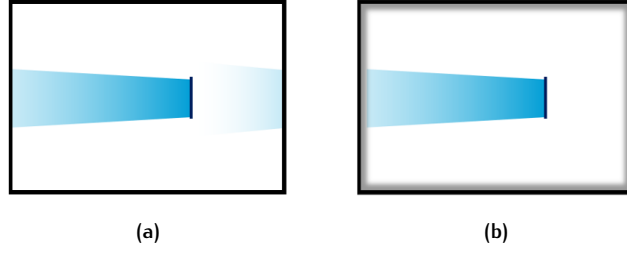


Figure 2.3: The boundary conditions as implemented in DALES with in (a) the original periodic boundary conditions and (b) the nudged boundary conditions. Modeled after a figure of Dorp [2016].

The nudging variable decreases the tendencies of the concentration of source ϕ : the original tendency before the nudging $\left. \frac{\partial \phi}{\partial t} \right|^{original}$ is multiplied with the nudging value f_{nudge} to obtain the nudged tendency. f_{nudge} increases gradually from 0 to 1 when a grid cell nears a boundary. Equations 2.35 and 2.36 give the implemented equations in DALES.

$$\left. \frac{\partial \phi}{\partial t} \right|^{nudged} = (1 - f_{nudge}) * \left. \frac{\partial \phi}{\partial t} \right|^{original} \quad (2.35)$$

where f_{nudge} is a matrix of size $(i_{tot} \times j_{tot})$, where all values with a distance to a boundary larger than d_{nudge} are zero. The entries inside the nudging depth distance from the boundary are calculated with:

$$f_{nudge} = \frac{1}{2} + \frac{1}{2} \cos \left(\frac{\pi}{d_{nudge}} i \right). \quad (2.36)$$

where i denotes the absolute distance in grid points from the closest boundary. When taken $d_{nudge} = 5$, figure 2.4 gives the calculated values of the domain. A cosine function is implemented to create a nudging gradient from 1 to 0 rather than a steep line, to prevent computational errors.

2.6 Advection

DALES gives the option of five different advection schemes. All advection schemes operate on with a global equation for advection in the x -direction is given as:

$$\frac{\delta \tilde{u}_i \phi_i}{\delta x} = \frac{F_{i+\frac{1}{2}} - F_{i-\frac{1}{2}}}{\Delta x}, \quad (2.37)$$

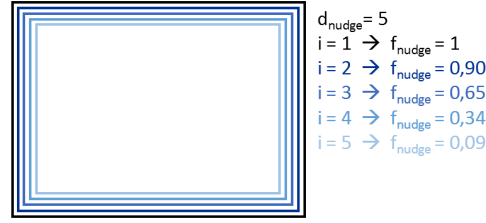


Figure 2.4: The calculated values of f_{nudge} at the edges of a domain with a nudge depth $d_{nudge} = 5$.

where $F_{i-\frac{1}{2}}$ represents the convective flux of ϕ through the plane $i - \frac{1}{2}$ perpendicular to the wind velocity \tilde{u}_i . The values of the convective flux $F_{i-\frac{1}{2}}$ are calculated by the one of the available advection schemes. In these equations ϕ can represent the variables $\tilde{u}, \tilde{v}, \tilde{w}, e^{1/2}$ or $\tilde{\varphi}$. The IBM module is currently only implemented for a second order advection scheme, for the reason that it is a relatively simple advection scheme:

$$F_{i-\frac{1}{2}}^{2nd} = \tilde{u}_{i-\frac{1}{2}} \frac{\phi_i + \phi_{i-1}}{2}. \quad (2.38)$$

The central difference in this equation can lead to negative concentrations, which lead to the addition of the Kappa advection scheme to DALES to prevent this problem. This scheme is modeled after the work of [Vreugdenhil and Koren \[1993\]](#), and is given as:

$$F_{i-\frac{1}{2}}^{\kappa} = \tilde{u}_{i-\frac{1}{2}} \left[\phi_{i-1} + \frac{1}{2} \kappa_{i-\frac{1}{2}} (\phi_{i-1} - \phi_{i-2}) \right]. \quad (2.39)$$

In this equation, $\kappa_{i-\frac{1}{2}}$ is defined as a switch that takes the magnitude of the upwind gradient of ϕ into account: a third-order upwind scheme when small, and first-order when stronger [[Heus et al., 2010](#)]. However, the IBM is not yet implemented for this advection scheme and therefore will only be used for a comparisons without IBM.

2.7 Addition of heterogeneous emission sources

The current version of DALES only allows the application of pollutants to be homogeneous, indicating that the predefined source flux will be emitted from every surface point at an equal rate. To investigate the effect of objects on the dispersion in a stable boundary layer and convective boundary layer, a non-homogeneous source is preferred. A point or line source allows the results to show the vertical and horizontal reach of the pollutant.

Therefore, an additional module is written into DALES. The main purpose of this module is to read an input file similar to to input file needed for the IBM, where every source can be prescribed to grid point at the surface level. Consequently, the module prescribing the source fluxes to grid points is altered. Previously, the emission of the source was prescribed to every location at every timestep. To only prescribe the emission to the specified location, a conditional function is added. To explain the details of this function, first the outline of the input file needs to be described.

The required input file consist of a matrix with size $(i_{tot} \times j_{tot})$ representing the surface area expressed in grid points, where every location $a_{i,j}$ contains an integer in between zero and the total number of different sources. This can be defined in the settings for the simulations. This method allows the user to define the desired area of emissions, for all points with the same number represent the same scalar. Figure 2.5 gives an example of a part of an input file, where three sources are defined: two point sources (1 and 2) and one line source (3).

```

0 0 0 0 3
0 1 0 0 3
0 0 0 0 3
0 0 0 0 3
0 0 2 0 3

```

Figure 2.5: An example of the input file for the source locations.

The source fluxes are prescribed per source, per surface grid point in multiple loops. As explained before, with heterogeneous sources, every source is prescribed to every grid point. The input file provides a matrix where every source has a specific integer, and grid points without source are equal to zero, as seen in figure 2.5. The added conditional function only prescribes the source flux to grid point matching the index of the source flux. For example, there are 3 source fluxes at the locations given in figure 2.5, with $\text{flux}(1) = 3 \text{ g g}^{-1}\text{ms}^{-1}$, $\text{flux}(2) = 2 \text{ g g}^{-1}\text{ms}^{-1}$, and $\text{flux}(3) = 7 \text{ g g}^{-1}\text{ms}^{-1}$. The first flux will only be prescribed to the grid points which have a value of 1 in the input file, etc. and the emission rates (in $\text{g g}^{-1}\text{ms}^{-1}$) per grid point will be as given in figure 2.6.

```

0 0 0 0 7
0 3 0 0 7
0 0 0 0 7
0 0 0 0 7
0 0 2 0 7

```

Figure 2.6: An example of the emission rates in $[\text{g g}^{-1}\text{ms}^{-1}]$ for the source locations matching the example in figure 2.5.

3

Gaussian Plume Model

The goal of this study is to analyse the dispersion within an urban area of DALES simulations in non-neutral conditions. Unfortunately, verification with measurements is not yet possible and therefore a different approach in an attempt of validation is applied. The dispersion results of the simulations in DALES without obstacles are compared to the dispersion results of a widely used model: the Gaussian plume model. The influence of the objects is measured in comparison with the DALES simulations without obstacles. This chapter gives an explanation of the Gaussian plume model and an overview of the used equations and parameters.

A study by Pirhalla et al. [2021] compared the dispersion results of a Gaussian plume model with LES results and measurements, and concluded that close to the source (5 - 10m) the Gaussian plume model is not as accurate as the LES model, however, beyond that distance, the results of both are highly accurate, even though LES slightly underestimated the peak concentration.

The Gaussian plume model is a highly idealized model for homogeneous terrain conditions without obstacles, to estimate the downwind concentrations of an emission source. The investigated sources are one line source and three point sources.

3.1 Point source model

The Gaussian plume model for a point source is described with the following equation:

$$\chi(x, y, z) = \frac{Q}{2\pi u \sigma_y \sigma_z} \exp\left(-\frac{y^2}{2\sigma_y^2}\right) \left[\exp\left(-\frac{(z-H)^2}{2\sigma_z^2}\right) + \exp\left(-\frac{(z+H)^2}{2\sigma_z^2}\right) \right]. \quad (3.1)$$

Here, $\chi(x, y, z)$ is the concentration at distance x downwind of the source, and cross-wind distance y and height z . Q is the intensity of the source in mass per unit time, u the wind velocity, H the height of the release. The release height H in all simulations will be zero, as will the height z in all calculations, resulting in the following equation:

$$\chi(x, 0, 0) = \frac{Q}{2\pi u \sigma_y \sigma_z} \exp\left(-\frac{y^2}{2\sigma_y^2}\right) \left[2 \exp\left(-\frac{z^2}{2\sigma_z^2}\right) \right]. \quad (3.2)$$

The most important variables here are σ_y and σ_z , which are resp. the lateral and vertical dispersion coefficient. In the literature, there are multiple approaches to

these variables, several studies have compared these methods on the basis of their performance in rural and urban areas. The best performing method according to the literature is a combination of different approaches [Mao et al., 2020; Wu and Liu, 2018; Essa et al., 2011; Carrascal et al., 1993]. A power-law, distance dependent approach is used for the vertical dispersion, and the lateral dispersion is based on an angular half-width of the plume. Section 3.2.1 elaborates on the implemented equations and parameters for these variables.

3.2 Line source model

The line source Gaussian plume Model is approached in the same manner as the implementation of the line source in DALES; as several point sources in formation. This enables the possibility to match the LES-modelled line source exactly.

3.2.1 Dispersion equations

The used equations for σ_y and σ_z in the implemented Gaussian plume model are as follows:

$$\sigma_z = cx^d \quad (3.3)$$

$$\sigma_y = 465.116x \cdot \tan(\theta) \quad (3.4)$$

where θ is defined with the following equation:

$$\theta = 0.01745(a - b \cdot \ln(x)). \quad (3.5)$$

All parameters are dependable on the Pasquill stability, class ranging from very unstable or convective (A) to very stable (F), and parameters c and d are additionally dependent on the downwind distance x in km of the source. The values of these parameters are given table 3.1 and 3.2 below. The implemented values are corresponding with the values of stability class A for the convective boundary layer simulations and E for the stable boundary layer. Here, the stability class E is chosen and not F, because class F contains very little to no turbulence and is mostly reliant on small scale eddies. The Large-Eddy Simulation method is therefore not able to properly calculate these small eddies.

Class	Stability	Parameters	
		a	b
A	Very Unstable	24.1670	2.5334
B	Unstable	18.3330	1.8096
C	Neutral/Slightly unstable	12.5000	1.0857
D	Neutral/Slightly stable	8.3330	0.7238
E	Stable	6.2500	0.5429
F	Very stable	4.1667	0.3619

Table 3.1: Coefficients for equations 3.4 and 3.3, based on Singer and Smit (1968).

Class	x (km)	c	d
A	0.10-0.15	158.08	1.0542
	0.16-0.20	170.22	1.0932
	0.21-0.25	179.52	1.1262
	0.26-0.30	217.41	1.2644
	0.31-0.40	358.89	1.4094
	0.41-0.50	346.75	1.7283
	0.50-3.11	453.85	2.1166
	> 3.11	$\sigma_z = 5000$	
B	0.10-0.20	90.673	0.93198
	0.21-0.40	94.483	0.98332
	> 0.40	109.300	1.09710
C	> 0.10	61.141	0.91465
D	0.10-0.30	34.459	0.86974
	0.31-1.00	32.093	0.81066
	1.01-3.00	32.093	0.64403
	3.01-10.00	33.504	0.60486
	10.01-30.00	36.650	0.56589
	> 30	44.053	0.51179
E	0.10-0.30	23.331	0.81956
	0.31-1.00	21.628	0.75660
	1.01-2.00	21.628	0.63077
	2.01-4.00	22.534	0.57154
	4.01-10.00	24.703	0.50527
	10.01-20.00	26.970	0.46713
	20.01-40.00	35.420	0.37615
F	0.10-0.20	15.209	0.81558
	0.21-0.70	14.457	0.78407
	0.71-1.00	13.953	0.68465
	1.01-2.00	13.953	0.63227
	2.01-3.00	14.823	0.54503
	3.01-7.00	16.178	0.46490
	7.01-15.00	17.836	0.41507
	15.01-30.0	22.551	0.32681

Table 3.2: Coefficients for equations 3.4 and 3.3, based on Cramer (1979).

4

Set-up of the Simulations

The dispersion of emissions within DALES is simulated in two different boundary layer conditions: a convective boundary layer (CBL) representing the day, and a stable boundary layer (SBL) representing the night. Both simulations are performed with and without the addition of an urban area, to investigate the effect hereof on the boundary layer, and examine the possible differences in their impact on a SBL and CBL.

This chapter elaborates on the setup of the different simulations and the implemented initial boundary conditions. First, the simulation time and chosen domain size are described in section 4.1, followed by the inversion jump (section 4.2) and the virtual potential surface temperature fluxes, and the initial vertical profiles of the potential temperature (section 4.3). The initial geostrophic wind velocity and applied advection scheme are discussed in section 4.4, and the initial vertical profiles of the subgrid-TKE are discussed for both the stable and the convective boundary layer in section 4.5. Section 4.6 and 4.7 show the implemented elevation map and the source locations, respectively. This chapter concludes with an elaboration of the case whereafter the SBL simulation is modeled, and the differences between the two.

The stable boundary layer is modeled after the GABLS1 study, which stands for Global Energy and Water Cycle Experiment Atmospheric Boundary Layer Study, and simulates a verified stable boundary layer [Beare et al., 2006]. The GABLS1 study investigated different models simulating a SBL at different resolutions, and compared the outcomes. All input files and settings are available in DALES, and therefore this study has been chosen to use as a starting point for simulating a reliable SBL. Furthermore, the GABLS1 case is simulated in DALES and used as a validation model for the SBL simulation without obstacles. Therefore, their exact variables and the differences between this study's SBL simulation and the GABLS1 simulation will be described in section 4.8. The convective boundary layer is mainly achieved through the addition of a positive surface temperature flux.

4.1 Simulation time and domain size

The initial simulation time and horizontal domain size and resolutions are equal for all simulations, whereas the vertical domain size and resolution differs per stability. Firstly, all simulations should produce a sufficient amount of output to properly

study all the data. As most simulation models, DALES requires some initialization time before it reaches a steady state, which is generally two hours. A total simulation time of eight hours will provide sufficient data.

The horizontal domain size of a convective boundary layer often requires a relatively large number of grid points, and should be able to provide sufficient surface area for numerous obstacles. Therefore the number of grid points in both x -, and y -direction is chosen to be 160. The implemented elevations of obstacles in this study are based on an elevation map with a horizontal resolution of $\Delta x = \Delta y = 5\text{m}$. This results in a horizontal domain size of $800 \times 800\text{m}$.

The vertical resolution depends on the size of the simulated eddies. A stable boundary layer contains relatively smaller scale eddies than a convective boundary layer due to the lack of turbulence, and therefore requires a smaller vertical resolution. To resolve most of the small scale eddies, the ideal vertical resolution should be approximately 3m [Beare et al., 2006]. To model an adequate portion of an urban area, and to resolve sufficient amount of the turbulence, the vertical resolution of the SBL will be set to 3m. This is very similar to the vertical resolution of the DALES - GABLS1 case of 3.125m. The simulations with a convective boundary layer could be properly modeled with a coarser grid, and will therefore have a vertical resolution of $\Delta z = 5$ meters.

The boundary layer height and the increase hereof determines the required vertical domain size. Due to the higher intensity of turbulence in a CBL the boundary layer increases over time, while the boundary layer height of the SBL remains approximately constant through time. Therefore the CBL requires a larger vertical domain than the SBL. A rule of thumb is that the boundary layer height is maximally $\frac{2}{3}$ of the modeled height of the domain. The initial boundary layer depth in both SBL and CBL simulations is 100m, as is the GABLS1 case. As the boundary layer height of the SBL is expected to remain approximately constant throughout the simulation, a vertical domain size of 500m should be more than sufficient, which results in 166 grid points.

However, the vertical domain size of the convective boundary layer is limited by the relatively small horizontal domain size. To properly implement an urban area in the lowest part of the atmosphere, the vertical resolution should be relatively small, and is therefore set to 5m. The total amount of grid point should be in the same order of greatness as the amount horizontal grid points of 160. A vertical domain size of 900m is chosen, which equals 180 grid points.

4.2 Subsidence and inversion jump

Typically, a convective boundary layer can grow several kilometers during the day. However, due to the limited vertical domain and the requirement of a boundary layer depth, h_{bl} , of maximally two-thirds of the total vertical domain size, the boundary layer growth, $\frac{\partial h}{\partial t}$, is to be controlled. In this study, the growth of the boundary layer is restrained by an inversion jump at the top of the boundary layer and the subsidence; the slowly downward motion of air. The subsidence generally is a function of the height and the divergence of the large-scale horizontal wind. Here a more pragmatic approach is applied to ensure the boundary layer height remains within the simulated domain, where the subsidence is prescribed for every height. A typical value for the divergence is 10^{-5} s^{-1} , which is applied in the CBL simulations.

To determine the minimum inversion jump $\Delta\theta_v$, the boundary layer growth can be calculated with:

$$\frac{\partial h}{\partial t} = A \frac{\overline{w'\theta'}_{srf}}{\Delta\theta} + \overline{w}_h \quad (4.1)$$

$$\overline{w}_h = -Div * z \quad (4.2)$$

$$h_{bl} = h_0 + \frac{\partial h}{\partial t} * t \quad (4.3)$$

with $A = 0.2$, $\overline{w'\theta'}_{srf}$ the potential surface temperature flux, $\Delta\theta$ the inversion jump and \overline{w}_h the subsidence, which is a function of the divergence Div and the height z in meters (equation 4.2). The boundary layer height after a simulation of eight hours can be calculated with equation 4.3, where h_0 is the initial boundary layer height. With these equations, the boundary layer height after eight hours can be determined, if the value of $\overline{w'\theta'}_{srf}$ is known. This value is obtained by averaging the potential surface temperature flux of several test simulations with an attempted CBL. From this is concluded that a $\Delta\theta = 6K$ would ensure a boundary layer depth after a simulated time of 8 hours to stay below 600m (two thirds of the total vertical domain of 900m).

4.3 Surface temperature flux

The stable and the convective boundary layer are both achieved in DALES by prescribing a time-dependent large-scale forcings of a negative and positive surface heat flux respectively, in the form of an hourly prescribed potential surface temperature, which decreases or increases every hour. Both heat fluxes are derived from observations in Eindhoven of the Royal Netherlands Meteorology Institute (KNMI) of two clear summer days, August 16th and 17th of 2016. The course of the potential liquid surface temperature $\theta_{l,srf}$ is calculated from the measured temperature T with $\theta_{l,srf} = T \cdot \frac{p_0 R_{cp}}{p}$, and is given in figure 4.1. Here, the implemented surface values for the stable and convective boundary layer are given in light blue and dark blue respectively.

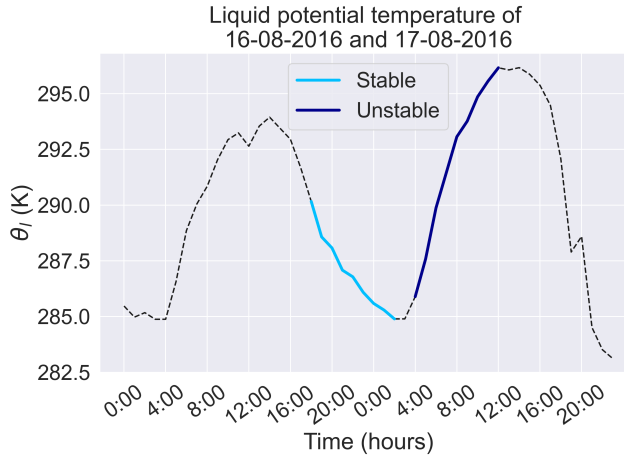


Figure 4.1: Course of the potential temperature $\theta_{l,srf}$ After which the CBL simulations are modeled.

DALES requires the initial vertical profile of the liquid potential temperature in one of its input files. This is constant throughout the stable boundary layer until the inversion height $z_i = 100m$ for both the SBL and CBL simulations. At the inversion height, in the CBL simulation θ_l will experience an inversion jump of $\Delta\theta = 6K$,

hereafter the potential temperature is a function of the height and the adiabatic lapse rate of 6 Kkm^{-1} :

$$z < z_i \longrightarrow \theta_l = \theta_0 \quad (4.4)$$

$$z \geq z_i \longrightarrow \theta_l = \theta_0 + \Delta\theta + \frac{6}{1000}z. \quad (4.5)$$

Here θ_0 denotes the potential liquid surface temperature at $t = 0\text{s}$, which is 290.16K in the SBL simulation and 285.89K in the CBL simulation derived from figure 4.1, and z is expressed in meters. The vertical profiles of both simulations are given in figure 4.2.

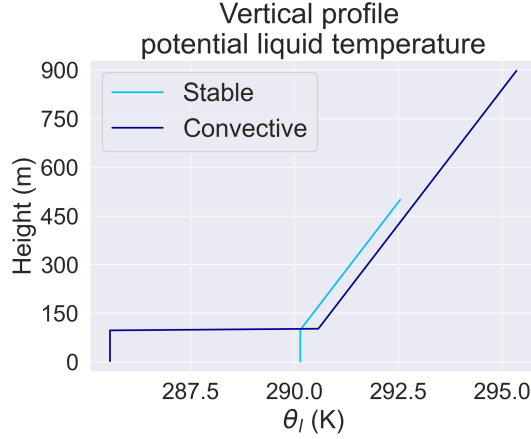


Figure 4.2: The vertical profile of the potential liquid temperature of the SBL and CBL simulations.

4.4 Initial geostrophic wind velocity and advection scheme

One of the most important prognostic variables is the initial geostrophic wind (geowind) velocity and direction. Both the SBL and CBL simulations are tested with several initial geowind velocities ranging from 2 ms^{-1} to 6 ms^{-1} . These tests showed that with an initial geowind velocity smaller than 5 ms^{-1} , the percentages of resolved turbulences with respect to the total turbulences become too small to speak of a properly resolved turbulent flow. Furthermore, wind velocities larger than 5 ms^{-1} reduced the desired differences between the stable and convective boundary layer, in terms of vertical component of the turbulent fluxes. Therefore, the initial geowind velocity for all simulations is 5 ms^{-1} .

To determine the wind direction, the locations of the sources and obstacles in the simulated urban area are examined, which are elaborated in section 4.7. From this is concluded that an Eastern wind is most desirable.

As described in section 2.6, there are several advection schemes available in DALES, with each its own advantages and disadvantages. Due to the fact that the IBM is only implemented for a second-order advection scheme, the four simulations (SBL with and without IBM, and CBL with and without IBM) will all be simulated with this advection scheme. The disadvantage of this advection scheme is the tendency to model negative concentrations. Therefore, an additional simulation without obstacles is performed of a stable boundary layer with a Kappa advection scheme to investigate the effect of a more advanced advection scheme on the dispersion.

4.5 Subgrid Turbulent Kinetic Energy

DALES requires a vertical profile of the initial subgrid turbulent kinetic energy (Subgrid-TKE). The Subgrid-TKE in both the stable and convective boundary layer are prescribed following the GABLS1 case, where the Subgrid-TKE is a function of the height z , while taking the inversion height z_i into account [Beare et al., 2006]. Above the inversion height, Subgrid-TKE = 0. Figure 4.3 shows the vertical profile of the implemented initial Subgrid-TKE values of both the SBL and CBL simulations.

$$z \leq z_i \longrightarrow \text{Subgrid-TKE} = 0.4 \left(1 - \frac{z}{z_i}\right)^3 \quad (4.6)$$

$$z > z_i \longrightarrow \text{Subgrid-TKE} = 0 \quad (4.7)$$

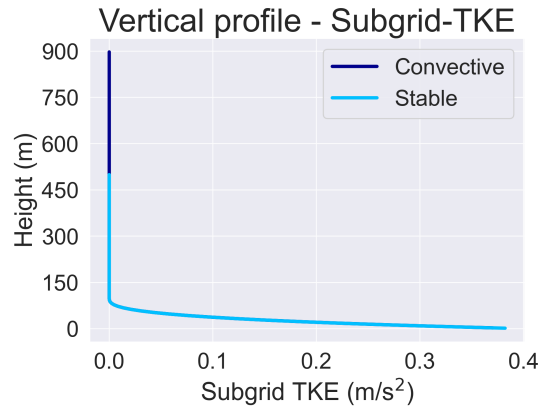


Figure 4.3: The initial vertical profile of the subgrid turbulent kinetic energy of the SBL and CBL simulations.

4.6 Surface boundary condition: implemented elevation map

To analyze the impact of objects on the dispersion, an elevation map of the city of Eindhoven is implemented. Several high-traffic streets are present near high buildings and residential areas, making this an interesting area to model the dispersion. Furthermore, there are two air quality measuring sites managed by the RIVM in Eindhoven, which locations are shown in figure 4.4a. Site A and B are respectively located at the Genovalaan and the Noord Brabantlaan. Location A is near a hospital and a shopping mall, making it an interesting location in terms of building heights. However, there is no large emitting source nearby, which is the case in location B. This measurement site is located near one of the main highways, which is known to be a large polluter. Therefore, all experiments will use an elevation map including this location, as figure 4.4b shows.

Multiple sections of the government have collaborated to a free to the public, elevation map, mapped from helicopter and airplane laser data: the AHN (Dutch: Actueel Hoogtebestand Nederland). These elevation maps are downloadable [here](#)¹ at the resolution of 0.5 or 5m. In figure 4.5a the original elevation map is shown, with vegetation, cars, and other irregularities. The dimensions used for this research

¹ Link: <https://downloads.pdok.nl/ahn3-downloadpage/>



Figure 4.4: a) Locations of the two measuring sites in Eindhoven, and b) the simulated location.

are five meters in the horizontal directions (x, y). Developers of DALES are currently working on incorporating vegetation in the model [Grylls and van Reeuwijk, 2021]. However, the version implemented here is incapable of modelling other structures than rectangle shaped object. Figure 4.5b shows the implemented elevation map of the stable boundary layer, corrected for obstacles other than buildings and layered per 5m.

The large circle-shaped object is the Evoluon in Eindhoven, and in figure 4.5a this is accompanied by a pond below street level. This pond and the part of the highway below street level ($h \approx 6.4$)m in the mid-left section of the figure, are shown at $h = 0$ m. In the DALES simulations, $h = 0$ m is located at the street, which explains the difference in height between the two figures.

The structures in this domain within five nodes from the boundary are removed, due to the nudging of the variables as explained in section 2.5.3.

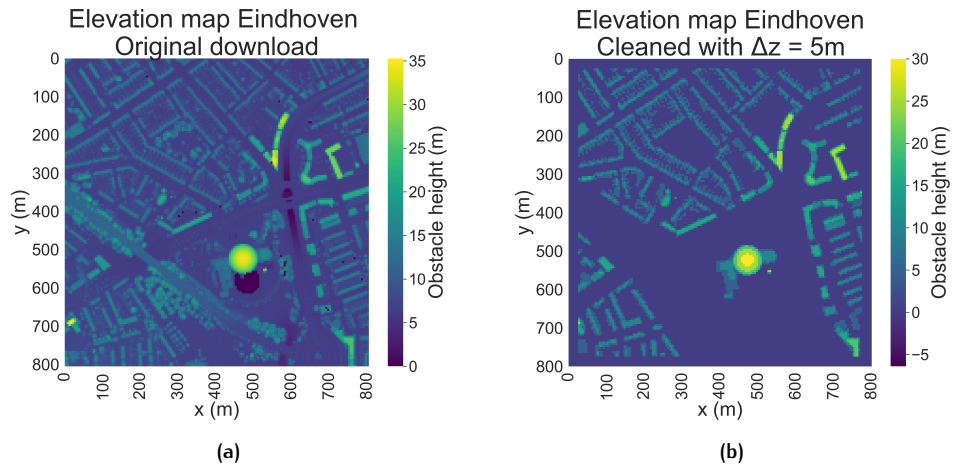


Figure 4.5: The elevation map of Eindhoven with location B at its center, (a) the original and (b) corrected for vegetation and formatted for the IBM input file.

4.7 Source locations

Two large highways are present in the simulated domain, and on the location of the Eastern highway, a line source is implemented, due to the Eastern wind direction. Around this line source are three point sources added, to investigate the dispersion of point sources, as well as line sources. Figure 4.6 shows their location with respect to the IBM map. One point source (location 2) is modeled in a relatively wide street in approximately the wind direction, the location of the next source (location 3)

is chosen at the same y -level as the measurement site, with respect to the wind direction. The last source (location 4) is located directly in front of the Evulon to investigate the dispersion of a point source with respect to a large, nearby building. The prescribed surface fluxes of the passive tracer are for all simulations and sources identical: $0.001 \text{ kg kg}^{-1} \text{ ms}^{-1}$, which is defined in the simulation settings.

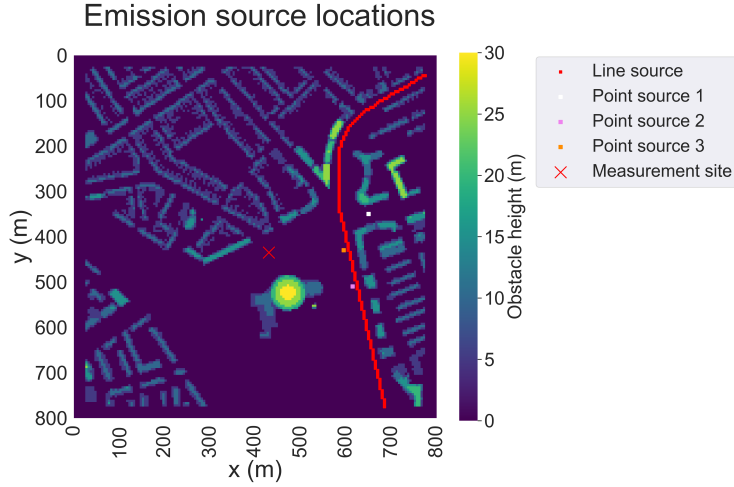


Figure 4.6: The locations of the scalars in the IBM domain.

4.8 Differences between the GABLS1 and this study's

SBL

The available GABLS1 has a dimension of $400 \times 400 \times 400 \text{ m}^3$ and a resolution of 3.125 m [Beare et al., 2006]. The vertical profile of the virtual potential temperature has a constant value of 265 K up to 100 m , and thereafter increases with 0.01 K m^{-1} . The initial geostrophic wind velocity in the East-West direction (u_{geo}) is equal to 8 ms^{-1} , and 0 ms^{-1} in the North-South direction (v_{geo}). A prescribed surface cooling of 0.25 Kh^{-1} is applied for 9 hours. The initial subgrid turbulent kinetic energy is a function of height: $0.4(1 - z/250)^3 \text{ ms}^{-2}$ for the first 100 m , after which it is equal to 0 ms^{-2} . The latter is equal to the initial subgrid-TKE values implemented in the SBL simulation for this study, whereas all of the other named variables differ. Table 4.1 gives an overview of the differences in the case of GABLS1 and the SBL simulation.

Case	Domain ($x \times y \times z$) [m^3]	Variable				
		$\Delta x = \Delta y$ [m]	Δz [m]	$\theta_{v,srf}$ [K]	u_{geo} [ms^{-1}]	$\partial\theta_{v,srf}/\partial t$ [Kh^{-1}]
GABLS	$400 \times 400 \times 400$	3.125	3.125	265	8	-0.25
SBL	$800 \times 800 \times 500$	5	3	290.16	5	-0.75

Table 4.1: Overview of the differences between the GABLS1 case and the implemented SBL for this study.

The differences in terms of domain size and resolution are due to the used elevation map and required horizontal domain for the convective boundary layer. The vertical resolution is deliberately similar with $\Delta z = 3 \text{ m}$. It is however taken slightly smaller to more accurately accommodate the buildings. Furthermore, the surface temperature differs significantly, because the simulation for this study is modeled

after a summers day in The Netherlands, setting the initial virtual potential surface temperature ($\theta_{v,srf}$) to 290.16K. Another result from the implementation of the measurements is the larger decrease in potential surface temperature over time, where the potential surface temperature of the GABLS1 simulation decreases with -0.25K per hour, the SBL simulation performed for this study decreases on average with -0.75K per hour.

Furthermore, the inversion height is identical, as is the adiabatic lapse rate from of the potential temperature above this inversion height om 100m and the vertical profile of the TKE. The wind velocity differs significantly, because a wind velocity of 8ms^{-1} would heavily influence the vertical dispersion in both the SBL an CBL simulation, decreasing the differences between the two.

The differences between these two cases will be extensively investigated in chapter 5.

5

Analysis of atmospheric conditions

To investigate DALES' capabilities to simulate an urban area faithfully, several steps are demanded. First, this chapter will analyse the SBL and CBL simulations without obstacles in section 5.1, to establish realistic simulated atmospheric conditions. As stated before, the stable boundary layer is constructed from the GABLS1 case [Beare et al., 2006], and several variables from the SBL simulation of this study will be compared against the results of the GABLS1 case. Even though both cases produce an SBL, the SBL simulated for this study will further be referred to as the SBL simulation. The convective cases will be verified by a theoretical approach, by analysing the vertical profiles of the buoyancy flux, TKE, velocity variances and the TKE budget equation.

When the reliability of the simulations is established, mainly in terms of the resolved turbulence and the velocity variances, section 5.2 will investigate the effect of the implemented urban area on the meteorological variables, like the vertical profiles of the wind velocity, and the buoyancy flux.

5.1 Establishing the simulations

The reliability of the simulated environment is analyzed by the results of several variables, the buoyancy flux, the vertical profiles of the total TKE and the SFS-TKE and the ratio between the two. The total buoyancy flux indicates the vertical kinematic flux of the virtual potential temperature, positive in the upwards direction. The vertical profiles of the TKE give insight into the magnitude of the simulated turbulence and the SFS-TKE ratio to the total TKE into the subgrid contribution to the total TKE, where a high value indicates a large dependency on subfilter turbulence. This variable is an important addition because a reliable simulation should not rely on subfilter turbulence.

5.1.1 Stable Boundary Layer (SBL)

As stated in chapter 4.8, the simulated SBL is based on the GABLS1 case, and the convective boundary layer is on surface measurements. To ensure a reliable SBL, the GABLS1 case is gradually modified to build the desired case. An elaboration

of the results of these simulations with on change per simulation are given in Appendix B. The largest differences between the GABLS1 case and the SBL simulation are the geostrophic wind velocity ($u_{geo,gabls} = 8\text{ms}^{-1}$ and $u_{geo,sbl} = 5\text{ms}^{-1}$), the initial surface temperature with a difference of 25K and the hourly decrease in surface temperature, where the surface temperature of the SBL simulation decreases three times as fast as the GABLS1 simulation.

Figure 5.1 gives the time-averaged vertical profiles of the buoyancy flux, the SFS and total TKE, and the ratio between the two, of both the GABLS1 and the SBL simulation. The buoyancy flux of both simulations are remarkably similar, following almost the same path. The only difference is that the total buoyancy flux of the SBL simulation at the surface is larger than the GABLS1 simulation, which can be explained by the larger hourly surface temperature decrease. The magnitude of the total TKE of both the simulations match as well. The vertical profile of the GABLS1 simulation however, contains more turbulence above 50m, where the SBL simulation decreases steadily with height, after the first levels. This difference could be due to the lower geowind, which in a stable boundary layer is one of the main causes of the turbulence, in the form of shear turbulence.

The subfilter-scale TKE of the SBL simulation is significantly smaller than the GABLS1 simulation, which in figure 5.1.b is behind the solid red line for the lowest heights. This translates to the ratios seen in figure 5.1.c, where the subgrid contribution to the total TKE is given. The SFS-TKE/Total TKE ratio of the GABLS1 case is relatively high, which indicates that most of the turbulence is not resolved, but parameterized. The ratio in the SBL simulation is smaller than 0.4, which is relatively small meaning that most turbulences are resolved.

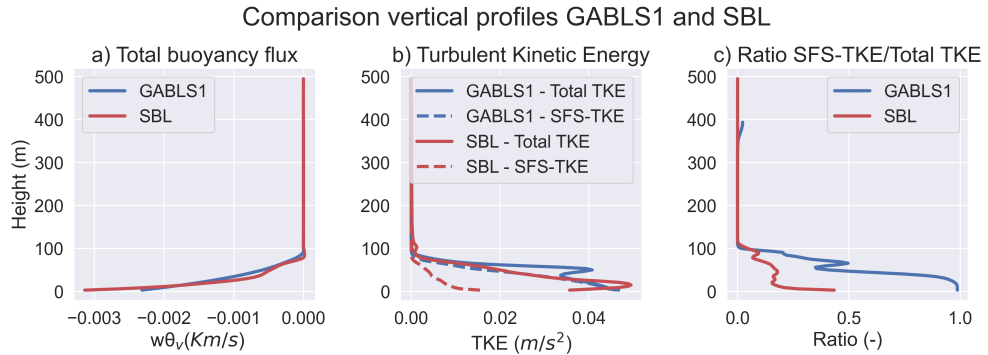


Figure 5.1: The vertical profiles of the total buoyancy flux, the total and SFS TKE and the ratio of SFS to Total TKE. Blue indicates the results of the GABLS1 simulation and red the SBL simulation.

From these results could be concluded that the simulated stable boundary layer is a reliable simulation, because of the favorable ratio of the subfilter surface TKE to the total turbulent kinetic energy, and the similar vertical profiles of the total TKE and buoyancy flux to the GABLS1 simulation.

5.1.2 Convective Boundary Layer (CBL)

The convective boundary layer is achieved with an increasing prescribed surface temperature to ensure the rise of the mixing layer. Due to the unaltered horizontal domain with respect to the SBL simulation ($800 \times 800\text{m}$), the vertical domain size is limited. The domain should be able to contain multiple eddies, and since their horizontal size is approximately equal to their vertical size, the boundary layer

depth is limited in its size and growth. The exact equations and values of the implemented subsidence to control the boundary layer growth are described in chapter 4.2.

Similarly to the SBL, the reliability of the CBL simulation is investigated through the total buoyancy flux, the resolved TKE and sub-filter scale TKE and their ratio, the resolved horizontal and vertical velocity variance and the TKE budget equation. Figure 5.2 shows the values of these variables over time, as the boundary layer grows with time.

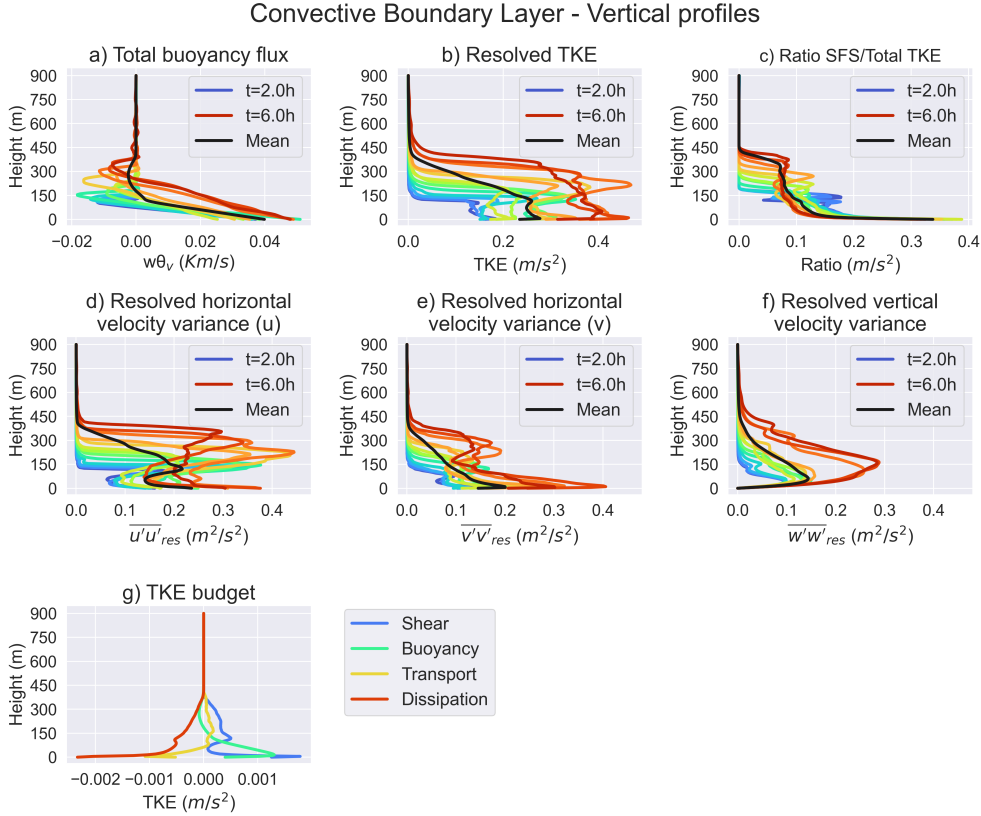


Figure 5.2: The vertical profiles of the total buoyancy flux, the resolved TKE, the ratio of SFS/Total TKE, the resolved horizontal and vertical velocity variance and the TKE budget equation, of the CBL simulation. The results range from $t = 2$ hours to $t = 6$ h, with blue the first timestep and red the last. If present, the solid black line gives the time-averaged value.

These figures show the growth of the boundary layer very clearly, starting with a height of 100m, developing slowly in these six hours to a boundary layer height of 600m. The last two simulated hours are discarded because the boundary layer grew beyond the 600m mark, creating unreliable results. First, the vertical profile of the buoyancy flux is following a vertical profile known to occur during the day: from a positive value on the surface, decreasing with height due to the excess in updrafts, to become negative in the mixing layer and thus having a decelerating effect on the rising of air parcels, and finally above the boundary layer, reaching a value of zero.

Furthermore, significantly more turbulence is resolved than parameterized as SFS-TKE, with an average SFS/Total TKE ratio in the boundary layer of 0.1. This indicates a well-performing simulation and a reliable convective boundary layer. The resolved horizontal and vertical variance all have comparable magnitudes, indicating sufficient turbulence in all directions, and follow the vertical profile as is expected of these variables and given in literature [Efstathiou et al., 2018]. The TKE-budget gives an indication of the main different components of the TKE. The buoyancy,

shear and transport factors are significantly enough to balance the dissipation from the resolved turbulence to small-scale eddies.

5.2 Effect of the addition of obstacles

In this section, the implementation of an urban area to a DALES simulation is analyzed through several variables, focusing on the impact on boundary layer height, buoyancy, the horizontal and vertical velocity variances and the TKE budget terms. The goal of this chapter is to examine whether DALES simulates a reliable urban area and give insights into topics requiring further investigation. This section starts with a first impression of the surface level concentrations with the addition of obstacles. This is followed by the expectations, and two separate analyses of several meteorological variables of the SBL simulation and the CBL simulation, to investigate the impact of obstacles of the simulated boundary layer. The two different boundary layers will be compared with each other in chapter 6.

The time-averaged surface concentrations of the line source are given in figure 5.3, of the SBL simulation with obstacles. Here can be seen that the concentrations within the buildings are zero and the fluxes flow properly around the obstacles.

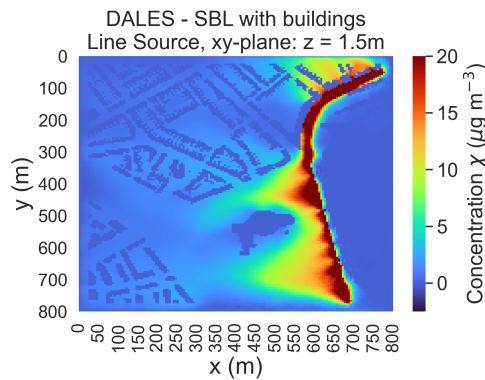


Figure 5.3: The time-averaged surface concentrations of the line source of the SBL simulation with obstacles.

5.2.1 Expectations

The expected influence of an urban area on a boundary layer regardless of the stability, is that the presence of buildings increases the boundary layer height. The horizontal turbulent fluxes at the building heights experience a change in direction when encountering a building by going around and above.

The expected effect on a stable boundary layer would be larger than the effect on a convective boundary layer. Considering that a convective boundary layer already has a strong vertical turbulence caused by convection, whereas the addition of a vertical flux to the stable boundary layer can significantly increase the boundary layer height. A convective boundary layer typically grows to several kilometers during the day, where the addition of several buildings with a maximum height of 30m, probably does not impact the boundary layer depth significantly. However, the simulated CBL in this study has a maximum boundary layer depth under 600m, due to domain restrictions. Therefore the addition of an elevation map will probably

add significantly to the boundary layer depth of a CBL, though considerably less than to the SBL.

5.2.2 SBL results

In figure 5.4 is the impact of the use of the IBM (dotted lines) shown for the SBL simulation, from the first level without obstacles up to a height of 180m. As can be seen clearly in 5.4.a) the vertical profile of the wind velocity, the stable boundary layer increases exactly with a factor of 1.5 due to the addition of an urban area. This explains the difference in the virtual temperature profile, because it increases linearly to the top of the boundary layer. The surface temperature and the temperature above the boundary layer are equal, only the boundary layer differs and therefore the slope of θ_v in the boundary layer. The difference in boundary layer height also results in the shown difference in the buoyancy flux.

The horizontal velocity variance in the wind direction is a factor 10 larger than in the other two direction, which is expected in a stable boundary layer where shear turbulence mostly dominates. Remarkably, the addition of an urban area to the simulation does not significantly change the horizontal velocity variance in the wind direction near the surface. The largest differences are the $\overline{v'v'_{res}}$, and $\overline{w'w'_{res}}$ near the surface, which is caused by the presence of buildings. This results in a larger dispersion rate with the addition of obstacles.

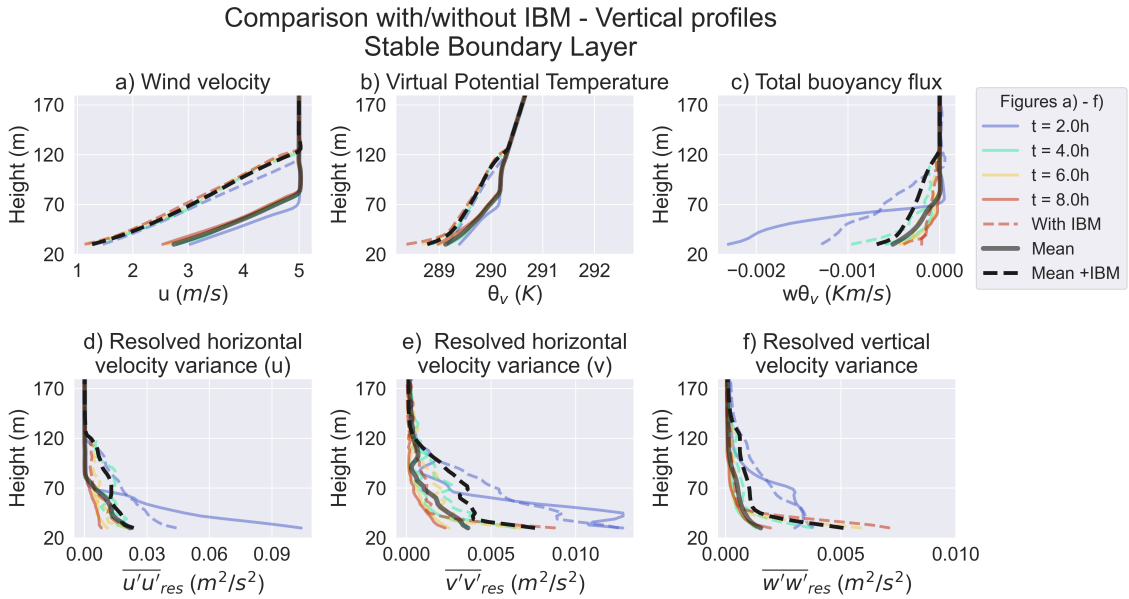


Figure 5.4: The impact of the obstacles on the stable boundary layer over time, expressed with the vertical profiles up to a height of 180m, of 4 different times in the simulation, and the average values in black. The dotted lines represent the simulations with obstacles and the solid line without. The following variables are shown: a) the wind velocity, b) the virtual potential temperature, c) the total buoyancy flux, d) and e) the resolved horizontal velocity variance in u and v direction respectively, and f) the resolved vertical velocity variance.

5.2.3 CBL results

The same calculations and figures as performed for figure 5.4 are repeated for the convective boundary layer. The results are shown in figure 5.5. Due to the constant growth of the boundary layer during this simulation, the time averaged values are not calculated for this analyses.

As expected, the boundary layer growth due to an urban area is not as significant for a convective boundary layer as a stable one. The convective boundary layer has grown with a factor of 1.12. Furthermore, figure 5.5.a) shows that with obstacles, the wind velocity in the boundary layer is significantly reduced, with the difference increasing over time. The presence of buildings halts the horizontal wind velocity in comparison with an area without buildings. However, it is remarkable to see the influence of buildings with a maximum height of 30m, have such a large impact on the wind velocity throughout the whole boundary layer. The impact of an urban area on a boundary layer of several kilometers is therefore an interesting topic to further investigate.

The slight difference between the two virtual potential temperature profiles is due to a larger upwards motion in the simulation with an urban area, therefore, the surface temperature is slightly better mixed with the boundary layer. With the addition of the obstacles, the buoyancy flux especially has a larger negative value indicating a larger mixing layer between the boundary layer and the free atmosphere above. The horizontal velocity variances in the wind direction (u) does not change near the surface, however the variances in the other two direction increase visibly in the lowest part of the atmosphere.

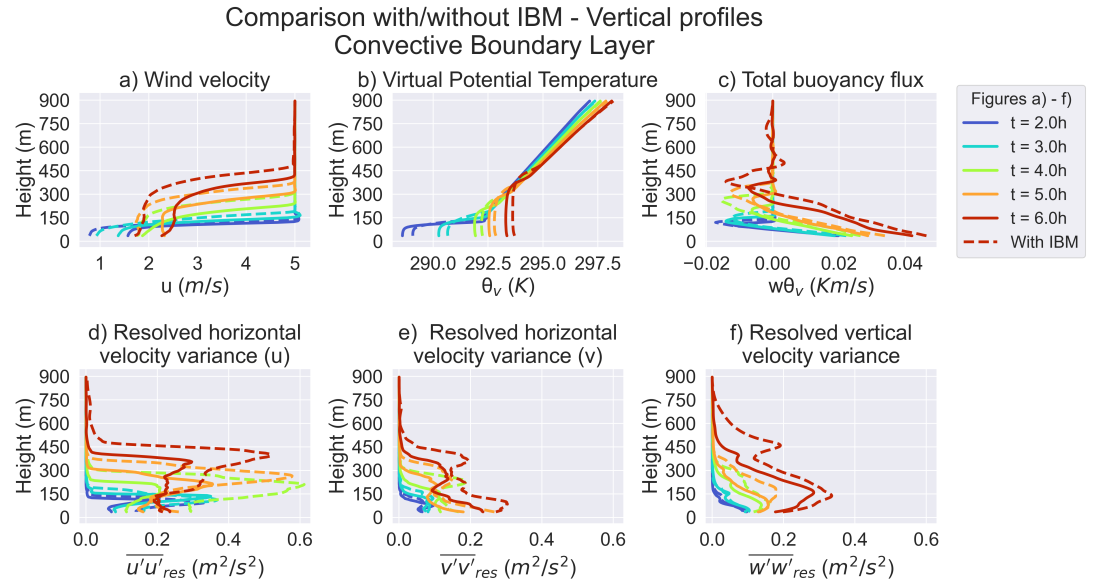


Figure 5.5: The impact of the obstacles on the convective boundary layer over time, of 4 different times in the simulation ranging from $t = 2\text{h}$ to $t = 6\text{h}$. The dotted lines represent the simulations with obstacles and the solid line without. The following variables are shown: a) the wind velocity, b) the virtual potential temperature, c) the total buoyancy flux, d) and e) the resolved horizontal velocity variance in u and v direction respectively, and f) the resolved vertical velocity variance.

6

Dispersion analysis

The diffusion of a pollutant in the atmosphere is directly related to the stability and thus the amount of turbulence. For this study the prescription of heterogeneous sources at the surface level is added to DALES, which allows the implementation of multiple sources, in this case one line source and three point sources, located at the surface. The in-depth description of this extra module and the locations of these sources is given in chapter 2.7 and 4.7 respectively.

First, the time-averaged concentrations of the pollutant of the simulations without obstacles are compared to the Gaussian plume model. They will be compared in the vertical as well as the horizontal plane, for both the stable and the convective boundary layer. Thereafter, the influence of the obstacles on the dispersion of the pollutant is inspected to assess the usability of DALES to properly model an urban area. This chapter gives the results for the line source, and the results for the point sources are given and elaborated in Appendix C, due to the fact that the results from the point sources are considerably similar to the results from the line source. Therefore, these analyses did not lead to different conclusions.

Finally, in section 6.3 two additional analyses are performed to investigate whether a different advection scheme has a significant influence on the dispersion. All time-averaged values do not take the first two hours into consideration due to the spin up of the simulation.

6.1 Comparison with the Gaussian plume model

The time-averaged concentrations of the SBL simulations without obstacles, of both DALES and the Gaussian plume model, are displayed in figure 6.1. The results are all scaled equally, and to ensure visibility at larger distances limited to a value of $20\mu\text{g}/\text{m}^3$, which is lower than the maximum concentration. The left figures show the concentration in an x - y -plane at the lowest obtained level, $z = 1.5\text{m}$, and the figures on the right give a height slice in the downwind direction, of the lowest 100m.

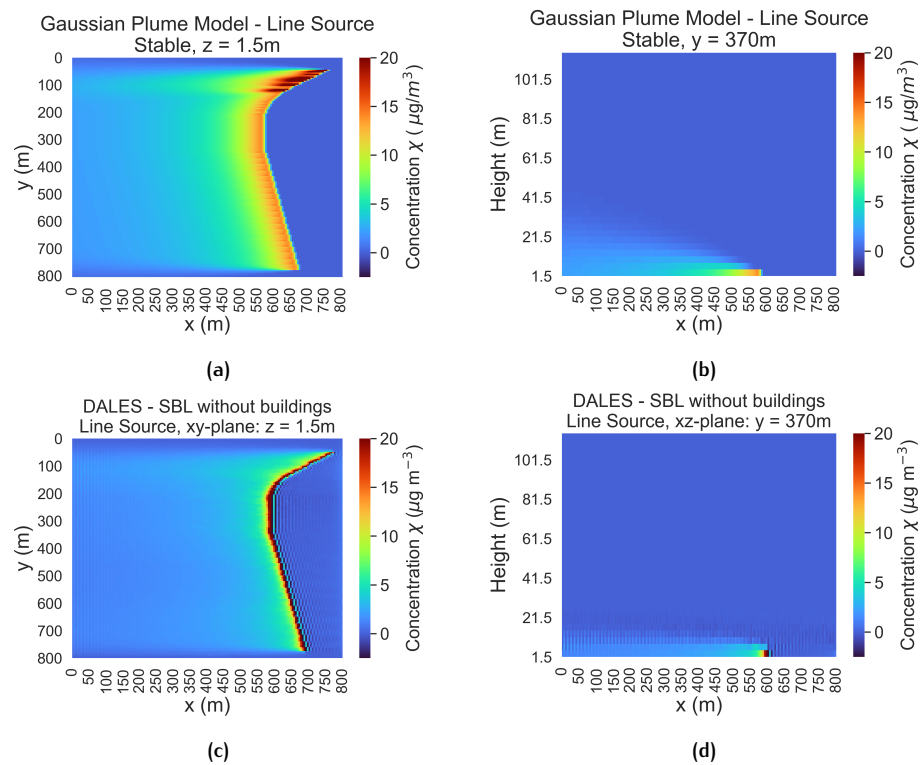


Figure 6.1: A visualisation of the pollutant concentration of the DALES and Gaussian plume SBL simulations, horizontally at $z = 1.5\text{m}$ and vertically downwind.

The concentrations of both the Gaussian plume model and DALES have a similar magnitude, however the concentration within the Gaussian plume model reaches higher into the boundary layer than simulated by DALES. Furthermore, the horizontal distribution downwind of the concentration differs between the two models. The results obtained by DALES have higher concentration at the source, while the Gaussian plume results show higher concentrations at larger distances.

Figure 6.1d shows an oscillating effect of the concentration upwind and above the plume, resulting in negative concentrations. This is due to the implemented advection scheme. Chapter 6.3 gives a more in-depth analysis of this aspect.

Figure 6.2 repeats the procedure as 6.1 for the CBL simulations. Immediately noticeable is the difference in magnitude of the concentrations. The concentrations obtained from the Gaussian plume model are significantly larger than obtained from DALES. This will be further investigated in this chapter. The downwind and upwards distribution of the concentrations however, seems to correspond quite well.

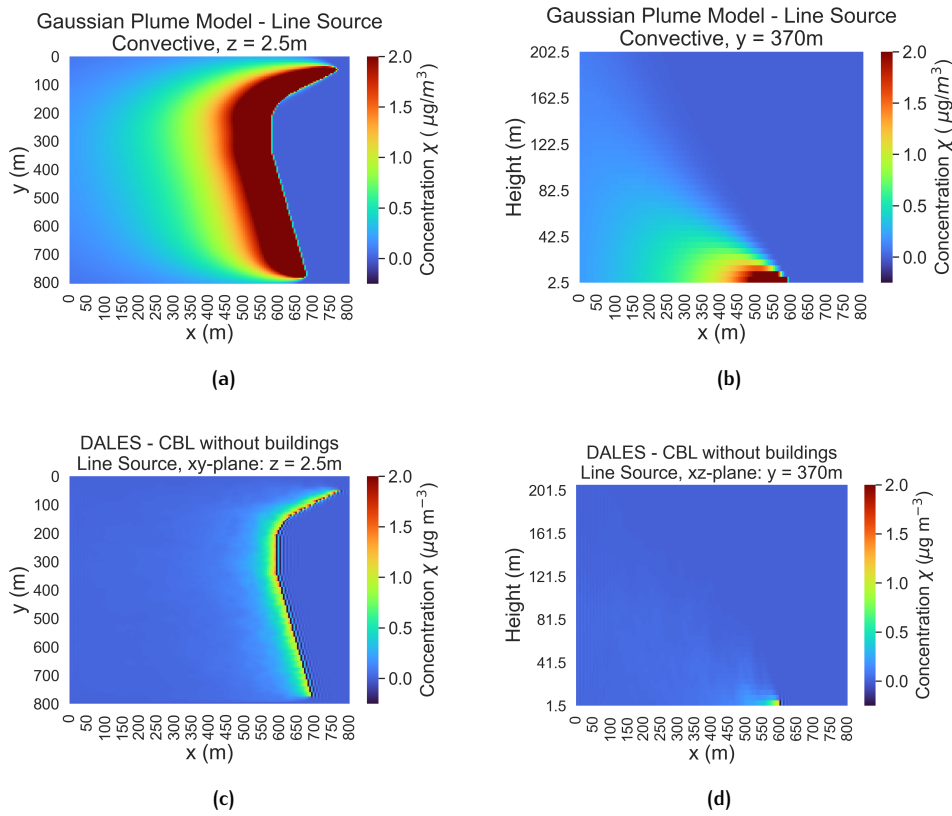


Figure 6.2: A visualisation of the pollutant concentration of the DALES and Gaussian plume CBL simulations, horizontally at $z = 2.5$ and vertically downwind.

6.1.1 Surface concentrations

In figure 6.3, the spatial distribution of the downwind concentrations are displayed, expressed with the actual concentrations in $\mu\text{g m}^{-3}$ and in percentages. The latter is calculated as the part of the sum of all directly downwind concentrations, calculated in percentages. E.g.: in figure 6.3.b., approximately 8.7% of all emitted downwind concentrations obtained by the Gaussian plume model is present at the source, whereas in the DALES results, this is $\approx 2.1\%$. The results of all simulations are shown, grouped per stability, at the surface level ($z = 0\text{m}$), time-averaged and averaged over for all x -values along the black lines in figure 6.5.

This figure gives insight into the concentrations at the lowest modeled elevation. As seen in figure 6.1 and 6.2, the concentrations of the SBL simulations are quite similar, apart from the concentrations at and close to the source. The Gaussian plume model calculates a higher concentration directly at the source, however, from 5m downwind of the source DALES calculates a higher surface concentration. These differences could be due to the fact that a Gaussian plume model is essentially build for sources with a certain stack height from the ground, where in this study the stack height equals 0m. The model first determines the locations downwind and the distances in x and y direction from the source, and then calculates the concentrations with a fixed set of parameters. The calculation of the concentration follows this parameterization and includes a double height term following the reflection assumption (see chapter 3 for further elaborations and the applied equations). This could cause such a high concentration at the source in the Gaussian plume model.

Concentrations, source at $x = 0\text{m}$ - Line source
 SBL: $z = 1.5\text{m}$, CBL: $z = 2.5\text{m}$

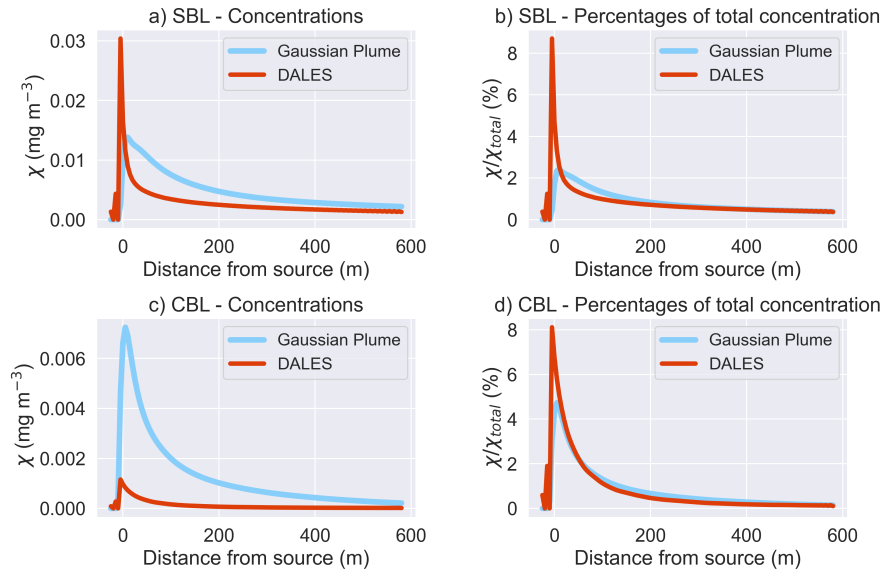


Figure 6.3: The time-averaged line source concentrations χ in the downwind direction and the percentages of the total concentration per downwind distance. The blue lines represent the results of the Gaussian plume model, red the DALES simulation without an urban area. a) and b) give the concentration and the percentages of the SBL simulations, and c) and d) of the CBL simulations.

The differences between the two CBL simulations are however more significant. The maximum concentration obtained from the convective Gaussian plume model is almost 10 times larger than the maximum concentration simulated by DALES. The spatial distribution of the CBL simulations however is significantly similar.

Figure 6.4 gives an equally scaled comparison of the SBL and CBL concentrations of both models, and shows that the concentrations of the SBL and CBL calculated by the Gaussian plume model differ with a factor of approximately 2, while the difference in DALES between the concentrations of the SBL and CBL simulations are a factor 10 apart. A reason for these differences in surface concentrations could be that most of the emission modeled by DALES disperses upwards instead of remaining at the surface. This will be further investigated in this section.

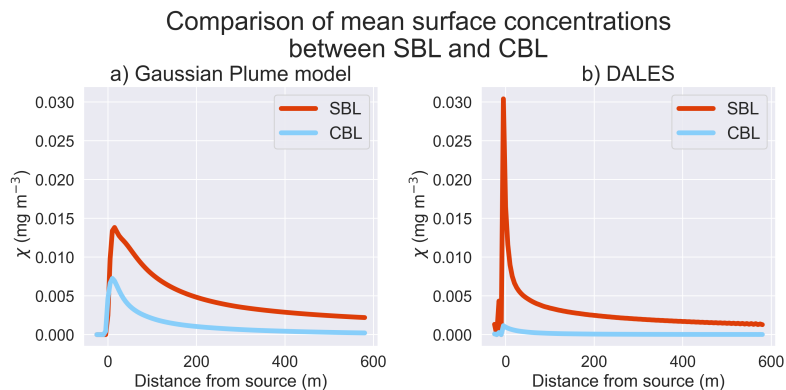


Figure 6.4: A comparison between the concentrations at downwind distances from the line source between the SBL and CBL simulations of a) the Gaussian plume model and b) DALES.

In conclusion, there are several significant differences between the surface concentrations of the Gaussian plume model and the DALES simulations of a line source pollutant. The distribution of the surface concentrations in a SBL is more evenly distributed in the downwind direction when simulated by DALES. The Gaussian plume model has a relatively high concentration at the source, but lower concentrations downwind than DALES calculates. For the CBL, the distribution of the downwind concentration of both simulations are more alike. However, the magnitude of the calculated concentrations differ considerably for this simulated boundary layer: the concentrations calculated by the Gaussian plume model are a factor of 10 larger than the surface concentrations obtained by DALES. The immense difference between the surface concentrations of the CBL simulation and the distribution of the SBL could be further investigated. The vertical distribution of the pollutant could be an explanation, and will be investigated in the next section.

6.1.2 Vertical profiles

The vertical profiles of the concentrations are analyzed at specific downwind distances from the line source. For practical reasons, this paragraph starts with an overview of these locations with respect to the line source. Figure 6.5 displays the location of the line source at 0m, and the concentrations are analyzed along the solid black lines, from $\Delta x = -5\text{m}$ to $\Delta x = 500\text{m}$. Here the time-averaged surface concentration levels of the passive scalar are shown of the stable boundary layer, with and without the buildings. Here the purpose of this figure is merely to reiterate the exact line source location and to provide a visual aid to the analyses.

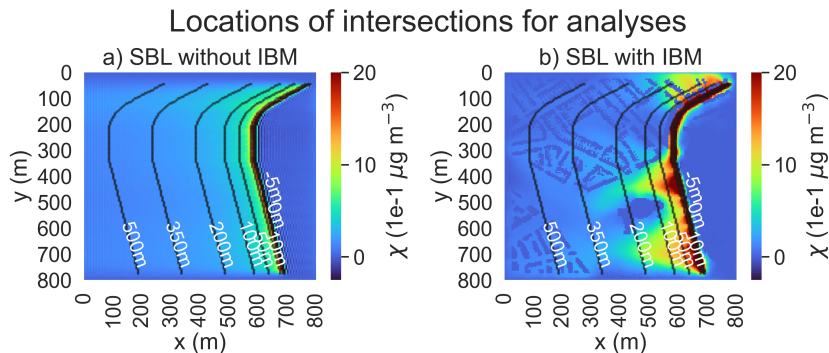


Figure 6.5: An informative figure for better understanding of the performed analyses in this chapter. Shown are the time-averaged surface concentrations ($z = 1.5\text{m}$), of the DALES - SBL simulations, with and without obstacles.

All analyses containing specific downwind distances from the source Δx are averaged over the black lines in figure 6.5. For example, if the vertical profile 200m from the source is given, is this the average of all concentrations along the black line denoted with 200m in figure 6.5, excluding the buildings if present. Furthermore, these lines specify which distances are analyzed.

In figure 6.6 the vertical profiles of the time- and spatial-averaged concentration are shown of the lowest part of the atmosphere. On the left are the DALES simulations without obstacles, and the results from the Gaussian plume model are portrayed on the right. The specific maximum height shown is dependent on the stability, 23m for the SBL simulations and 45m for the CBL simulations. As discussed in the previous paragraph, the surface concentrations in the Gaussian plume model are considerably higher for a CBL than calculated by DALES. Seen in this figure, is that this is also true for the vertical profiles of the concentration.

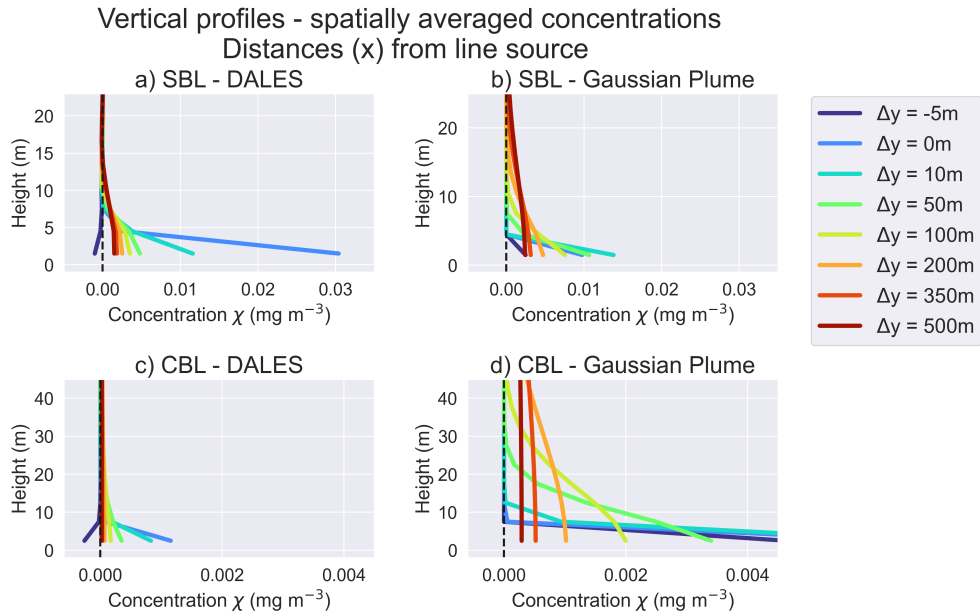


Figure 6.6: The time-averaged, spatial averaged, vertical profiles of the concentration as obtained from the DALES and Gaussian plume model at several downwind distances from the line source, as shown in figure 6.5. a) and b) give the concentration and the percentages of the SBL simulations, and c) and d) of the CBL simulations.

The vertical profile of the SBL simulation differs considerably between the two models. The concentration in the Gaussian plume model reaches higher elevation than the concentrations obtained from DALES. In both the stable and convective boundary layer, most of the concentration remains at the surface, and the surface concentrations of the SBL are significantly higher than the CBL.

6.1.3 Development over time

Figure 6.7.a. and b. show the development over time of both the DALES simulations without the immersed boundary method compared to the Gaussian plume model, at several predefined distances from the source. The concentrations calculated by the Gaussian plume model are constant due to the constant input variables of the emission rate Q and the wind velocity. All concentration are shown at $z = 1.5\text{m}$ for the SBL and $z = 2.5\text{m}$ for the CBL. DALES takes approximately two hours to initiate the simulation, this is denoted with a dotted grey line in both figures. Interesting is the increase at $t = 2\text{h}$, followed by a decrease, and a steady increase again in concentration over time in the stable boundary layer at all distances from the source, whereas in the convective boundary layer, the concentration oscillates around a stable amplitude. From this could be concluded that in a stable boundary layer, a percentage of the emission will remain close to the source instead of dispersing out of the domain. In a convective boundary layer, this does not seem the case.

6.1.4 Conclusion

There are considerable differences between the calculated diffusion of the two models, in terms of magnitude, the vertical and horizontal distribution, especially in the CBL simulation. The magnitude of the concentrations in the CBL differs considerably while the horizontal and vertical distribution are quite similar, they only differ

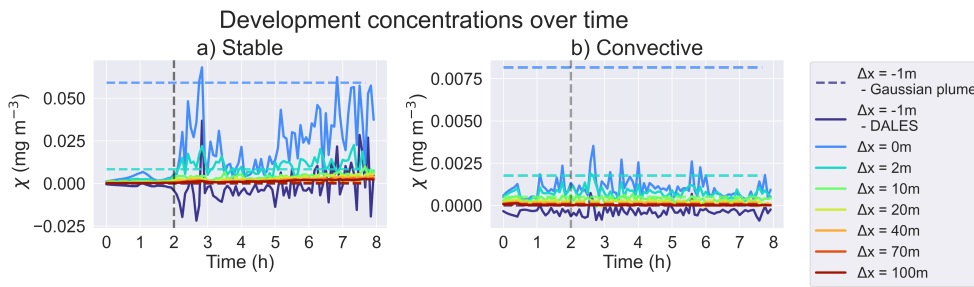


Figure 6.7: The Development of the concentration over time of the Gaussian plume model and a) the simulated stable boundary layer and b) the simulated convective boundary layer.

with a factor of 10 in magnitude. The dispersion in the SBL simulations are more similar, however, DALES calculates a higher value at the surface, but lower downwind and reaches a lower height than in the Gaussian plume model. Remarkable is the large difference in concentrations between the stable and convective boundary layer, which are significantly larger between the two DALES simulations than the Gaussian plume calculations. All these factors contribute to the conclusion that more research is necessary to investigate the diffusion profiles of a line or point source in DALES in comparison with the Gaussian plume model.

6.2 Comparison with the urban area

The effect of the added obstacles on the diffusion of an pollutant is investigated with the same analyses as performed in the previous section. Figure 6.8 gives a global insight into the concentration distribution of SBL and CBL simulations performed by DALES. Similarly to 6.1, the left figures are the horizontal distributions of the concentrations at the $z = 1.5\text{m}$ for the SBL and $z = 2.5\text{m}$ for the CBL, and the vertical distributions are shown at the right.

These figures immediately show a considerable impact of the obstacles on the surface concentrations. Moreover, these figures display that the implementation of an urban area in DALES seems to function properly, when looking at dispersion. The concentrations of the passive tracer move around the obstacles and the maximum value of the concentration is not only centered at the source, but more evenly distributed around the source.

Another observation is that in both the SBL and CBL the emission seems to stay in the lowest part of the atmosphere and concentrates around the source, downwind and upwind. It does reach a higher altitude in a city, due to the upwards motion of the fluxes corresponding with the presence of buildings. The effect is larger in a stable boundary layer, however the IBM seems to still have a significant impact on the surface concentrations. Further investigation into these values is performed in following sections.

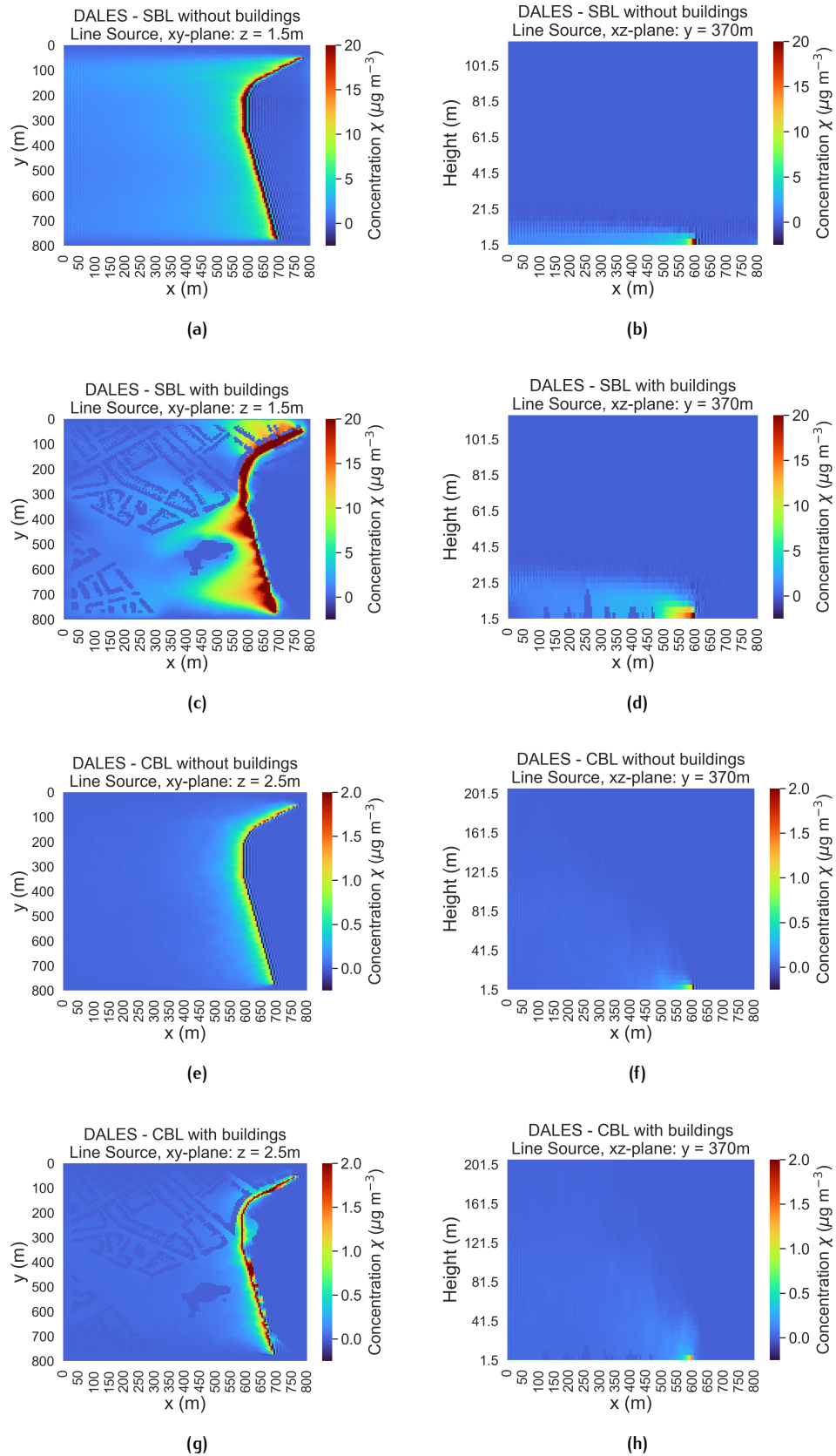


Figure 6.8: Vertical and horizontal profiles of time-averaged concentrations of the SBL and CBL DALES simulation, with obstacles and without.

6.2.1 Surface concentrations

Figure 6.9 displays the horizontal distribution of the surface level concentrations of the SBL and CBL simulations, comparing the results with and without obstacles. The locations where a building is present are excluded.

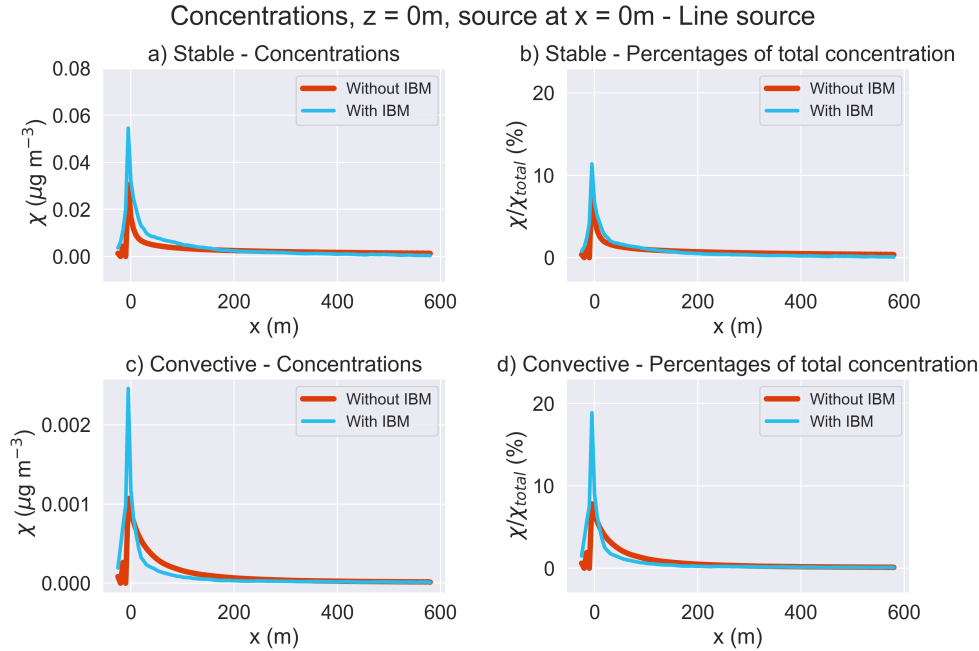


Figure 6.9: A comparison of the time-averaged line source concentrations χ between the simulation with (blue) and without obstacles (red). These values are the averaged in the downwind direction and the percentages of the total concentration per downwind distance. a) and b) give the concentration and the percentages respectively of the SBL simulations, and c) and d) of the CBL simulations.

As expected, this figure shows that the surface concentrations levels are much more concentrated when surrounded by buildings. The concentration at the source of the stable boundary layer has increased with a factor of 1.8 and the concentration in the convective layer with 2.3. In the SBL simulation, the concentrations at a short distance from the source are increased by the presence of the obstacles, while in the CBL simulation, this is not the case. This is probably due to the increase of turbulence present in the convective boundary layer, resulting in an increased concentration at higher elevations. This effects also applies to the horizontal distribution of the concentration.

6.2.2 Vertical profiles

As introduced before, figure 6.10 given the vertical profiles of the concentrations, spatially averaged along the line source, at several distances from the source location. Here can be seen that not only have the obstacles a large impact on the horizontal diffusion, it also influences the vertical distribution of a tracer concentration. Moreover, without obstacles the concentrations upwind are negative, while figure b) and d) show that the concentration upwind at $\Delta x = -5\text{ms}^{-1}$ is nearly as high as downwind. The concentration in the simulations without obstacles is more concentrated around the source, regardless of the stability. However, at further distances from the source, the concentration levels decreases when an urban area is added. In the SBL simulation, this effect is seen after 200m, while in the CBL

simulation, the concentrations obtained by DALES with obstacles are lower from a downwind distance of 50m.

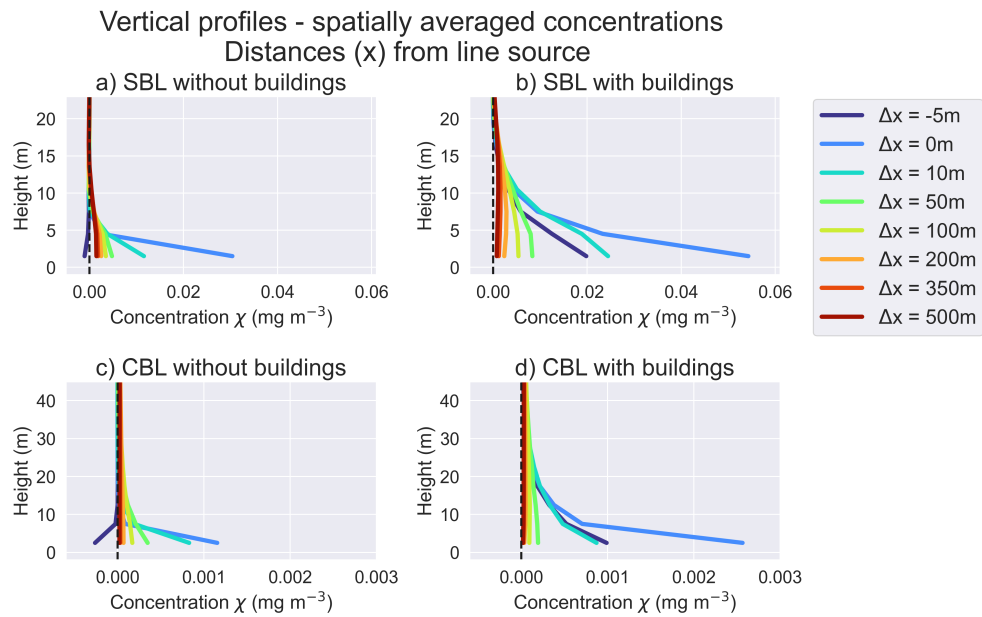


Figure 6.10: Vertical profiles of the concentrations within the stable and convective boundary layer, with and without IBM at several downwind distances from the line source.

Figure 6.11 gives the vertical distributions expressed as the part of the sum of the vertical concentration per height, of both the SBL and the CBL simulation. E.g.: at 0m from the source location (figure 6.11.a), the simulation without buildings (blue) calculated that approximately 90% of the all the vertically distributed concentrations are present at the surface level ($z = 1.5\text{m}$). All blue lines denote the simulation without buildings, and red with buildings. This metric is introduced to compare the vertical distributions if the absolute concentration values differ greatly in their magnitude, as per the CBL simulation.

Here the effect of the obstacles can clearly be seen, as that even at the source location ($\Delta x = 0$) the percentage of the total vertical concentration at the surface is 54%, whereas in both the stable and convective boundary layer without an IBM, this percentage is nearly 90%. Interesting is the development of dispersion in the stable boundary layer with distance, where at $\Delta x = 500\text{m}$, the most concentration is not at the surface, but rather at $z = 25\text{m}$. This effect is also seen in the convective boundary layer, at $\Delta x = 100\text{m}$, however less significant.

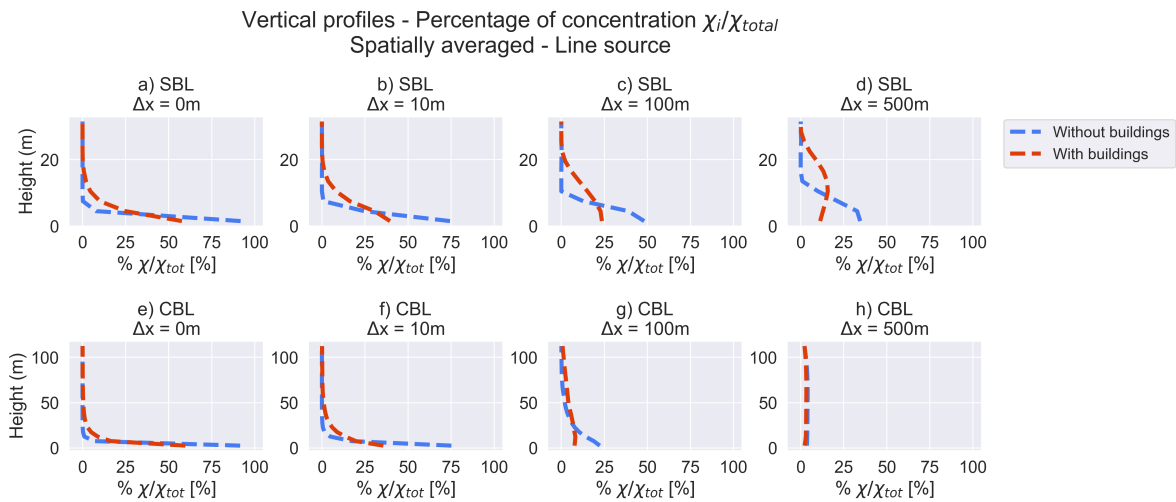


Figure 6.11: Vertical distribution of the concentrations within the stable and convective boundary layer of both the simulations with and without an IBM, at several distances from the line source.

6.2.3 Development over time

Figure 6.12 gives an overview of the development of the surface concentrations over time. The SBL simulation without obstacles has, from $t = 5h$ an increase with time, as has the SBL simulation with obstacles from distances larger than 10m from the source. All simulations have a considerable large oscillation effect. On a stable boundary layer, the addition of the urban area, have on both the SBL as the CBL an enlarging effect on the surface concentration of the passive tracer.

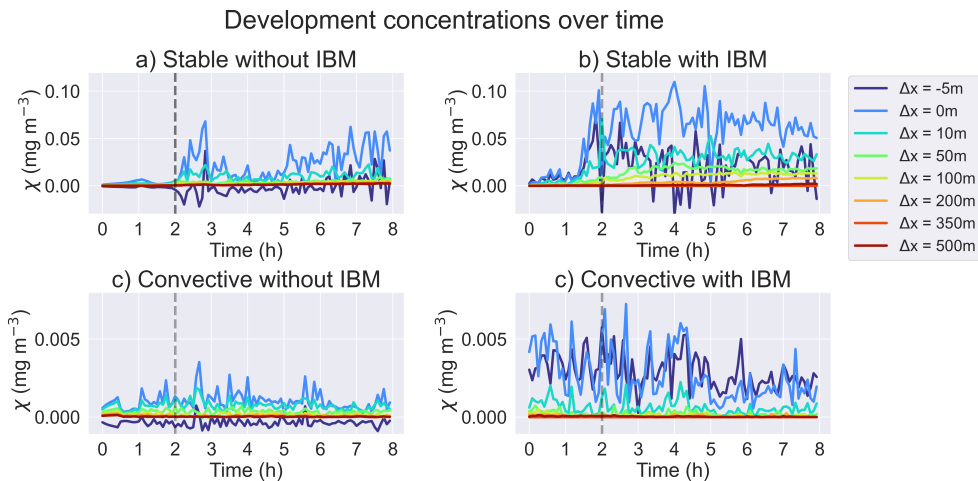


Figure 6.12: The Development of the surface concentration over time of the stable (a. and b.) and the convective (c. and d.) boundary layer. The different colors denote the different downwind distances from the source.

6.2.4 Conclusion

The surface concentration of a pollutant is severely influenced by the presence of buildings, regardless the stability of the atmosphere. The effect is smaller on the time-averaged concentrations in stable night-time conditions, than convective day-

time conditions. The concentration can grow with a factor of 1.5 – 5 times the concentration without an urban area, depending on the distance and height from the source. The dispersion is restrained by the presence of buildings within 200m in a stable boundary layer and 50m in a convective boundary layer. These results are presumably highly dependent on the wind velocity, placing of buildings and source, vertical domain size, and turbulence. These factors require further investigation to advance the study of the implementation of an urban area in DALES.

Furthermore, the addition of the urban area has a significant impact on the development of the downwind surface concentrations over time in the stable boundary layer. Whereas the downwind surface concentrations increase over time in the stable boundary layer without buildings, the presence of buildings has a large impact on these concentrations.

6.3 Influence of a different advection scheme

As explained in chapter 2.6, DALES offers the option to implement different advection schemes. The Immersed Boundary Method which provides the addition of an urban area, is only implemented for a second order advection scheme. However, as seen in the results earlier this chapter, this advection scheme can cause an oscillating effect in some fluxes.

An additional simulation is performed to investigate the influence of a different advection scheme on the dispersion, the kappa advection scheme. This simulation is in all aspects identical to the stable boundary layer simulation without the addition of obstacles, with one difference: the advection scheme. This simulation will be referred to in this chapter as the Kappa simulation. Figure 6.13 gives the vertical and horizontal distribution as obtained from the three models; the DALES simulation with a Kappa advection scheme, the DALES simulation with a second order advection scheme and the Gaussian plume model. Only the SBL simulations is investigated. The left figures give the horizontal distribution at the surface level ($z = 1.5\text{m}$) and the right figures give the vertical distribution.

The distribution of the pollutant as calculated by the kappa advection scheme seems to resemble the Gaussian plume model to a greater degree, with a higher concentration at the source and a lower concentration downwind. The implementation of this advection scheme has resolved the oscillation present in the simulation displayed in 6.13.c and d.

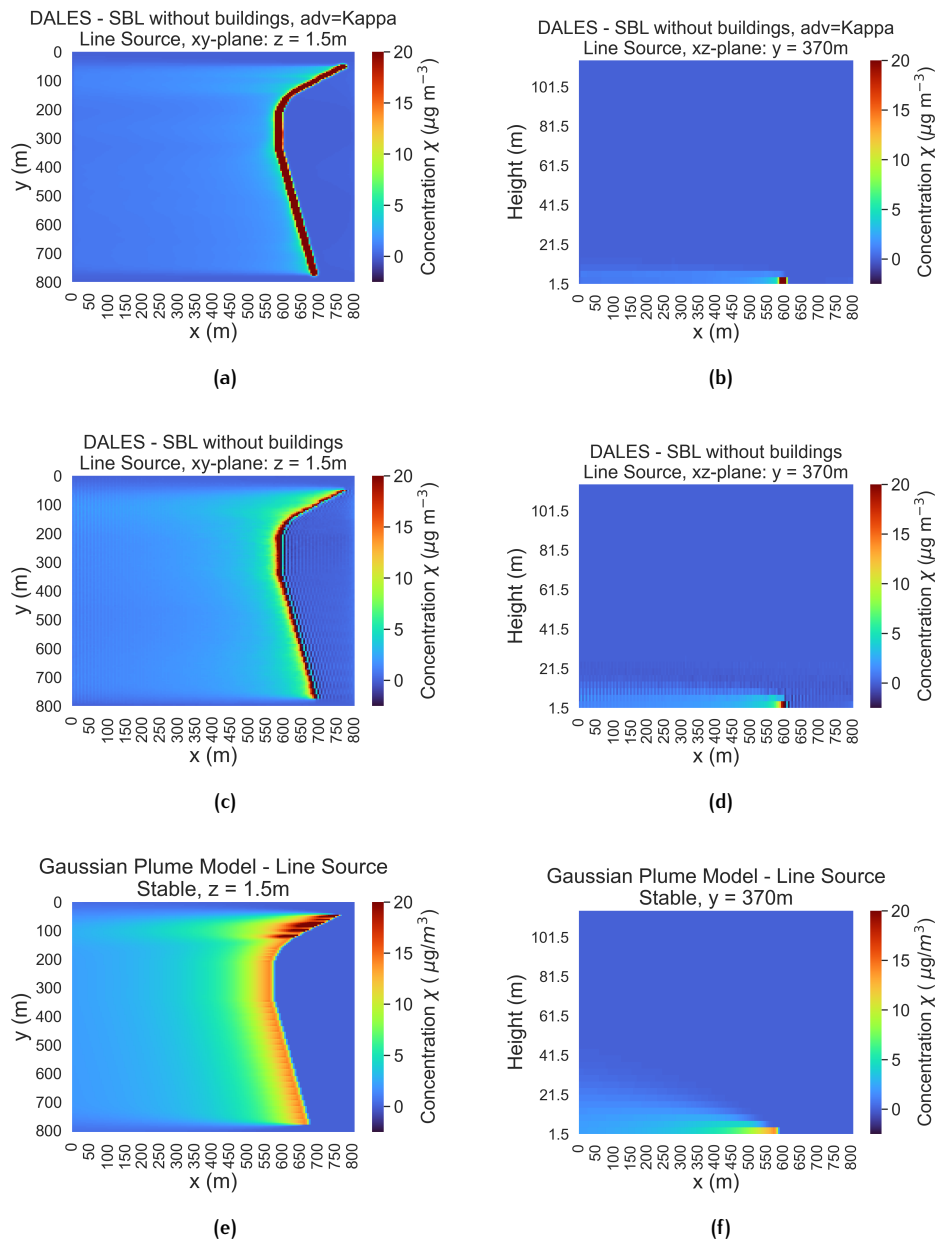


Figure 6.13: Vertical and horizontal profiles of time-averaged concentrations of the Kappa advection scheme, in comparison to the second order advection scheme and the Gaussian plume model.

Interesting is to investigate the seemingly higher concentrations at the source in the DALES-Kappa simulation. Figure 6.14 gives these values, spatially- and time-averaged, with $x = 0$ the location of the source. Remarkable is the magnitude of the concentration at the source. The maximum value of the Kappa simulation is over 10 times the size of the second order-simulation and 6 times of the Gaussian plume. The distribution of the concentration over the downwind distance is almost identical to the Gaussian plume model, possibly indicating the correctness of both.

An explanation for the low concentrations calculated with the second order advection scheme could be that the oscillating effect possibly impacts the magnitude of the highest concentration. The concentrations fields within DALES are conserved, meaning that the presence of negative values impacts the size of the positive values. Therefore, with the absence of the negative values, the concentrations calculated in the Kappa-simulation are locally higher than calculated by the second order advective

tion scheme.

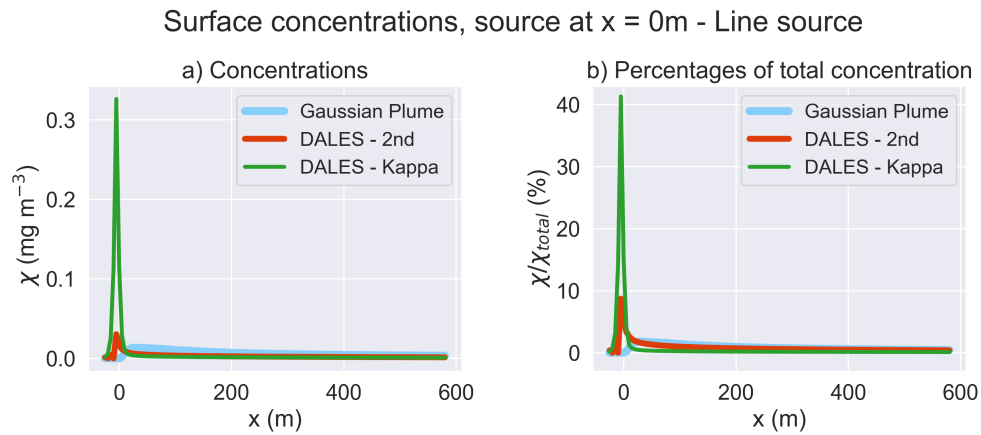


Figure 6.14: The surface concentrations of the SBL Gaussian plume model, the DALES simulation with a 2nd order advection scheme and the DALES simulation with a Kappa advection scheme.

Figure 6.15 displays the vertical distribution of the concentration at different downwind distances. From this graph can be concluded that the Kappa advection scheme has a minimal effect on the vertical diffusion. The surface values differ slightly, however, the overall distribution is remarkable similar. While the horizontal distribution resembles the Gaussian plume model, the vertical are significantly different.

These results show the difficulty in comparing the dispersion of a pollutant close to the source. LES may not be the best tool to investigate the concentrations at this distance. However, further downwind, it benefits in terms of spatial distributions, time variations and taking into account presence of obstacles.

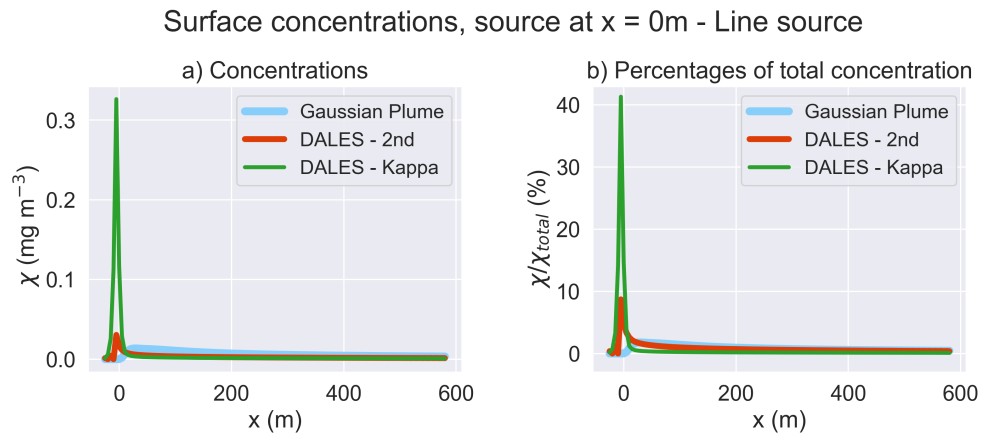


Figure 6.15: The vertical profile distribution of the Gaussian plume model, the Kappa advection scheme and the second order advection scheme, displayed at several downwind distances.

6.3.1 Development over time

In figure 6.16 the development of the surface concentrations over time are displays of the Gaussian plume model, the SBL DALES simulation without the implementation of the IBM, and the Kappa simulation at different distances from the source.

As seen before, the concentration at the source is significantly higher in the Kappa simulation, and increases heavily over time. Therefore, the same results are shown three times, on three different vertical scales. The development of the concentration over time at the Kappa simulation is experiencing almost no oscillation in both the absolute value and time, but increases steadily.

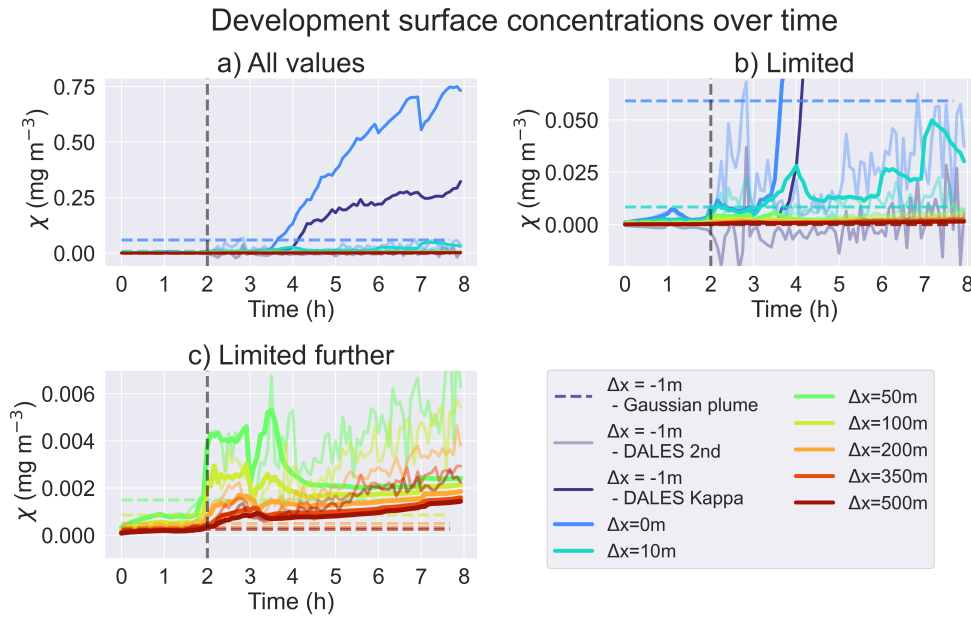


Figure 6.16: Development of surface concentrations over time of the simulation with the Kappa advection scheme, compared with the SBL simulation without obstacles and the Gaussian plume model

6.3.2 Conclusion

The kappa advection scheme is rather similar to the Gaussian plume model in terms of the horizontal distribution. The concentration at the source is considerably higher than the second order advection scheme, questioning the reliability of these values. Perhaps the oscillating effect observed with the second order advection scheme, meaning the erroneous negative values and positive values near the source, had an impact on the magnitude of the concentration. Therefore a favourable improvement to the DALES is the implementation of the kappa advection scheme in combination with the addition of obstacles. Additionally, the lack of oscillation and negative values in the concentration over time when calculated with the Kappa advection scheme given this advection scheme preference over the second order advection scheme.

7

Conclusions and Recommendations

This chapter concludes all findings in the analyses performed in chapter 5 and 6, followed by the recommendations for further studies. First the conclusion will inspect the effect of the addition of an urban area on different variables of the stable and convective boundary layer. This is followed by the conclusions of the dispersion analyses: the comparison with the Gaussian plume model and the influence of obstacles on the dispersion. The impact of a different advection scheme of the dispersion is discussed last. This chapter concludes with the recommendations for further studies.

7.1 Conclusions

7.1.1 Effect of the addition of obstacles

The impact of the obstacles is measured in terms of boundary layer height and the vertical profiles of the wind velocity, buoyancy flux and turbulence. The expected influence of an urban area on a boundary layer regardless of the stability, is that the presence of buildings increases the boundary layer height. The horizontal turbulent fluxes of the TKE at the building heights experience a change in direction when encountering a building by going around it. A part of the horizontal turbulence translates thus to the vertical turbulent transport. The simulation results show that the stable boundary layer height grows with 50%, while the convective boundary layer height increase with 12%.

In regard of the vertical wind velocity profile, the presence of buildings halts the horizontal wind velocity of both the stable and convective boundary layer, throughout the whole boundary layer almost with 50%. As the maximum height of the buildings in the simulated part of Eindhoven for this study is merely 30m, it is interesting that these relatively small buildings have such a large impact on the vertical wind profile.

7.1.2 Dispersion

First the DALES simulations without an urban area are compared to a Gaussian plume model, in terms of horizontal and vertical distribution and the development of the concentrations over time. Then the effect of the obstacles on the DALES simulations is assessed on the same aspects.

Gaussian plume comparison

There are considerable differences between the calculated diffusion of the Gaussian plume model and DALES, in terms magnitude for the CBL simulation, and the horizontal distribution for the SBL simulation. The concentrations calculated by DALES are approximately ten times smaller than calculated by the Gaussian plume model, while the concentrations between the SBL simulations of both models differ with a factor smaller than two. In the SBL simulation results of DALES, the surface concentration is larger at the source than the Gaussian plume model estimates, while further downwind, the surface concentration obtained by the Gaussian plume model is higher. Moreover, the concentration calculated by the Gaussian plume model reach a higher elevation in the stable boundary layer than simulated by DALES.

Effect of an urban area

The concentration of a pollutant is severely influenced by the presence of buildings, regardless the stability of the atmosphere. The effect is larger on the time-averaged concentrations in stable night-time conditions, than convective day-time conditions. The results of the simulations showed that the surface concentrations of the pollutant in the SBL where higher up to a downwind distance of 200m due to the presence of buildings, but after this distance the surface concentration decreased with respect to the SBL simulation without buildings. In a convective boundary layer, the downwind distance from which the surface concentration decreases due to the presence of buildings is much closer: 50m due to the larger turbulences present in the CBL. These results could be highly dependent on the wind velocity, placing of buildings and the source, vertical domain size, and turbulence. These factors require further investigation to advance the study of the implementation of an urban area in DALES.

Furthermore, the surface concentration calculated by DALES increases with time in a stable boundary layer, which needs further investigation. The development over time of the surface concentration in the CBL simulations do nu decrease nor increase over time.

Kappa advection scheme

The results as obtained by the simulation with the kappa advection scheme are rather similar to the Gaussian plume model in terms of the horizontal distribution. The concentration at the source is considerably higher than the second order advection scheme, questioning the reliability of these values. Perhaps the oscillating effect of the surface concentration observed with the second order advection scheme has an impact on the magnitude of the concentration. Therefore a favourable improvement to the IBM in DALES is the implementation of the kappa advection scheme in combination with an IBM. Additionally, the lack of oscillation in the concentration over time when calculated with the Kappa advection scheme given this advection scheme preference over the second order advection scheme. Similar to the second order advection scheme, the surface concentrations increase over time.

7.2 Recommendations

From these analyses, several aspects come to light which require further research. First, the impact of an urban area on a deep convective boundary layer is necessary to investigate whether the results observed in this study also apply there, such as the large impact on the boundary layer height and the vertical profile of the wind velocity.

The comparison between the Gaussian plume model, DALES and the results obtained from the two advection schemes illustrated the extremely large differences between magnitude of the simulated concentrations of the CBL and the SBL, and the horizontal and the vertical distribution of the concentrations. Additional investigation into the relevance of the stack height of the source is recommended. The addition of the line and point sources build for this study only allow the source to be located at the surface.

Finally, several additions and adjustments to DALES are needed to accurately simulate the dispersion of pollutions in a city: the possibility to simulate vegetation, and the possibility to add the building height as a 3D matrix instead of a birds-eye-view. Currently the top of the buildings are given in a 2D matrix and DALES assumes all grid-points below the top of the building as such. For the most part of an urban area a 3D matrix would not make a enormous difference as most of the buildings straight, and the data for a 3D matrix of a city is not to my knowledge available. However, for example the modeled Evoluon in this study, is spherical, and therefore the flow would be more realistic if a 3D matrix could be implemented.

Several aspects were out of scope for this research which should still be investigated. This research excluded any form of moisture in the atmosphere, which are very interesting topics: cloudiness and precipitation. The wind speed and direction could also be differentiated, to investigate their effect on the dispersion.

Bibliography

- Ascenso, A., Augusto, B., Silveira, C., Rafael, S., Coelho, S., Monteiro, A., Ferreira, J., Menezes, I., Roebeling, P., and Miranda, A. I. (2021). Impacts of nature-based solutions on the urban atmospheric environment: a case study for eindhoven, the netherlands. *Urban Forestry and Urban Greening*, 57. Cited By :1.
- Beare, R. J., Macvean, M. K., Holtslag, A. A., Cuxart, J., Esau, I., Golaz, J.-C., Jimenez, M. A., Khairoutdinov, M., Kosovic, B., Lewellen, D., et al. (2006). An intercomparison of large-eddy simulations of the stable boundary layer. *Boundary-Layer Meteorology*, 118(2):247–272.
- Carrascal, M. D., Puigcerver, M., and Puig, P. (1993). Sensitivity of gaussian plume model to dispersion specifications. *Theoretical and Applied Climatology*, 48(2-3):147–157. Cited By :22.
- Deardorff, J. W. (1974). Three-dimensional numerical study of the height and mean structure of a heated planetary boundary layer. *Boundary-Layer Meteorology*, 7(1):81–106.
- Deardorff, J. W. (1980). Stratocumulus-capped mixed layers derived from a three-dimensional model. *Boundary-Layer Meteorology*, 18(4):495–527.
- Dorp, P. v. (2016). Large-eddy simulation of wind farms in clear and cloud-topped boundary layers.
- Efstathiou, G. A., Plant, R. S., and Bopape, M.-J. M. (2018). Simulation of an evolving convective boundary layer using a scale-dependent dynamic smagorinsky model at near-gray-zone resolutions. *Journal of Applied Meteorology and Climatology*, 57(9):2197–2214.
- Essa, K. S., Ghobrial, R. A., Mina, A., and Higazy, M. (2011). Calculation of cross-wind integrated concentration by using different dispersion schemes. *Mausam*, 62(1):51–60.
- Grylls, T., Suter, I., and van Reeuwijk, M. (2020). Steady-state large-eddy simulations of convective and stable urban boundary layers. *Boundary-Layer Meteorology*, 175(3):309–341. Cited By :3.
- Grylls, T. and van Reeuwijk, M. (2021). Tree model with drag, transpiration, shading and deposition: Identification of cooling regimes and large-eddy simulation. *Agricultural and Forest Meteorology*, 298:108288.
- Heus, T., Van Heerwaarden, C. C., Jonker, H. J. J., Pier Siebesma, A., Axelsen, S., Van Den Dries, K., Geoffroy, O., Moene, A. F., Pino, D., De Roode, S. R., and De Arellano, J. V. . (2010). Formulation of the dutch atmospheric large-eddy simulation (dales) and overview of its applications. *Geoscientific Model Development*, 3(2):415–444. Cited By :133.
- Jia, H. and Kikumoto, H. (2021). Source term estimation in complex urban environments based on bayesian inference and unsteady adjoint equations simulated via large eddy simulation. *Building and Environment*, 193.
- Koene, M. (2020). Implementation of ibm in dales.

- Letzel, M. O., Krane, M., and Raasch, S. (2008). High resolution urban large-eddy simulation studies from street canyon to neighbourhood scale. *Atmospheric Environment*, 42(38):8770–8784.
- Lilly, D. K. (1967). The representation of small-scale turbulence in numerical simulation experiments. *Proceedings of IBM Scientific Computing Symposium on Environmental Sciences*, Edited by: Goldstine, H. H.:195–210.
- Mao, S., Lang, J., Chen, T., Cheng, S., Cui, J., Shen, Z., and Hu, F. (2020). Comparison of the impacts of empirical power-law dispersion schemes on simulations of pollutant dispersion during different atmospheric conditions. *Atmospheric Environment*, 224. Cited By :2.
- Nieuwstadt, F. and Brost, R. (1986). The decay of convective turbulence. *Journal of Atmospheric Sciences*, 43(6):532–546.
- Pirhalla, M., Heist, D., Perry, S., Tang, W., and Brouwer, L. (2021). Simulations of dispersion through an irregular urban building array. *Atmospheric Environment*, 258.
- Resler, J., Krč, P., Belda, M., Juruš, P., Benešová, N., Lopata, J., Vlček, O., Damašková, D., Eben, K., Derbek, P., et al. (2017). Palm-usm v1.0: A new urban surface model integrated into the palm large-eddy simulation model. *Geoscientific Model Development*, 10(10):3635–3659.
- Smagorinsky, J. (1963). General circulation experiments with the primitive equations: I. the basic experiment. *Monthly weather review*, 91(3):99–164.
- Sommeria, G. (1976). Three-dimensional simulation of turbulent processes in an undisturbed trade wind boundary layer. *Journal of Atmospheric Sciences*, 33(2):216–241.
- Tomas, J., Pourquie, M., and Jonker, H. (2016). Stable stratification effects on flow and pollutant dispersion in boundary layers entering a generic urban environment. *Boundary-Layer Meteorology*, 159(2):221–239.
- Tominaga, Y., Mochida, A., Murakami, S., and Sawaki, S. (2008). Comparison of various revised k- models and les applied to flow around a high-rise building model with 1:1:2 shape placed within the surface boundary layer. *Journal of Wind Engineering and Industrial Aerodynamics*, 96(4):389–411.
- Verzijlbergh, R., Jonker, H., Heus, T., and Vilà-Guerau de Arellano, J. (2009). Turbulent dispersion in cloud-topped boundary layers. *Atmospheric Chemistry and Physics*, 9(4):1289–1302.
- Vreugdenhil, C. B. and Koren, B. (1993). *Numerical Methods for Advection-Diffusion Problems*, volume 45. Vieweg.
- Walton, A. and Cheng, A. (2002). Large-eddy simulation of pollution dispersion in an urban street canyon—part ii: idealised canyon simulation. *Atmospheric Environment*, 36(22):3615–3627.
- WHO, W. H. O. (2016). *World health statistics 2016: monitoring health for the SDGs sustainable development goals*. World Health Organization.
- Wu, Z. and Liu, C. . (2018). Source depletion analogy for reactive plume dispersion over schematic urban areas. *Atmospheric Environment*, 190:226–231. Cited By :2.
- Xie, Z.-T., Coceal, O., and Castro, I. P. (2008). Large-eddy simulation of flows over random urban-like obstacles. *Boundary-layer meteorology*, 129(1):1–23.

- Xie, Z.-T., Hayden, P., and Wood, C. R. (2013). Large-eddy simulation of approaching-flow stratification on dispersion over arrays of buildings. *Atmospheric Environment*, 71:64–74.
- Yang, G., Li, X., Ding, L., Zhu, F., Wang, Z., Wang, S., Xu, Z., Xu, J., Qiu, P., and Guo, Z. (2019). Cfd simulation of pollutant emission in a natural draft dry cooling tower with flue gas injection: Comparison between les and rans. *Energies*, 12(19).



Inputfiles for the DALES simulations

DALES requires several inputfiles in order to perform a simulation properly, with the file-type ASCII. The settings are given in file called namoptions, and several initial vertical profiles are given in 'prof.inp' and 'lscale.inp', where the later contains the large scale forcings. The large scale fluxes causing the convective of stable boundary layer are prescribed to dales in the file 'ls_flux'. The different settings between the SBL and the CBL are noted as such.

A.1 Settings - namoptions

```
&RUN
iexpnr = 001
lwarmstart = .false.
runtime = 28800 (s)
irandom = 43
randthl = 0.1
randqt = 0
nsv = 4          number of passive scalars: 1 line source and 3 point sources
ladaptive = .true.
```

```
&DOMAIN          all specifications containing the domain size
itot = 160       amount of horizontal grid points in x-direction
jtot = 160       amount of horizontal grid points in y-direction
kmax = 167       amount of vertical grid points
xsize = 800.     domain size in x-direction (m)
ysize = 800.     domain size in y-direction (m)
```

```

&PHYSIC
ltimedep = .true.      setting to include timedependent fluxes
lmoist = .false.      no moisture
iradiation = 0        no radiation
lcoriol = .false.     no coriolis force
wsvsurf = 0.001, 0.001, 0.001, 0.001
                        prescribed surface scalar flux (kg kg-1 ms-1)

```

```

&NAMSURFACE
z0 = 0.1
ps = 101900.00 (Pa)
isurf = 2
thls = SBL: 290.16, CBL: 285.98 (K)
wqsurf = 0 (kg kg-1 ms-1)

```

```

&DYNAMICS
llsadv = .false.
lqlnr = .false.
cu = 0.
cv = 0.
iadv_mom = 2, Kappa:7  advection scheme, 2 = second order, 7 = Kappa
iadv_tke = 2
iadv_thl = 2
iadv_qt = 2
iadv_sv = 2

```

```

&NAMSCALAR      additional settings for heterogeneous scalars
lscalar = .true. switch to implement the scalar module
lboundary = .true. switch to nudge turbulent fluxes at domain edges
nudgetdepthgr = 5 number of nodes from domain edges from which
                    the nudging is applied

```

The addition of obstacles:

```

&NAMRURALBOUNDARY
lruralboundary = .true. switch to implement the IBM module
ldefrural = .true.      input file with the obstacle height is prescribed
lnoslip = .false.
lwallfunc = .true.
lfluxform = .true.
lpoislast = .true.
lthlwalltimedep = .true. switch to depend the wall temperature on the
                          prescribed timedependent temperatures
thlwall = SBL: 290.16, CBL: 285.98 (K), initial wall temperature of
                          buildings
ct = 0.

```

A.2 Vertical profiles - prof.inp

This inputfile contains the initial vertical profiles at the height of the half-nodes, e.g. the SBL simulation has a vertical resolution of 3m, thus the vertical profiles are specified starting from 1.5m, to 4.5m, etc., and For the CBL simulation with a $\Delta z = 5\text{m}$, the heights specified are 2.5m, 7.5m, etc.

The prescribed variables are the initial profiles of the liquid potential temperature θ_l (K), the total water specific humidity q_t (kg k^{-1}), the wind velocity in North-South direction (u) and East-West direction (v) in ms^{-1} , and the turbulent kinetic energy TKE in m^2s^2 . The vertical profiles of θ_l differs for the SBL and CBL simulations which are specified in chapter 4.3, as is the vertical profile of the TKE. This study does not take any moisture into account, resulting the $q_t = 0 \text{ kg k}^{-1}$ for all heights. The desired wind direction is East, making $u = 0 \text{ ms}^{-1}$ for all heights. The implemented initial wind velocity is 5 ms^{-1} , in the Eastern direction makes the value of v for all heights -5 ms^{-1} .

A.3 Large scale forcings - lscale.inp

The large scale forcings, such as the geostrophic wind velocity u_{geo} and v_{geo} and the subsidence are specified in this inputfile. The values of u_{geo} and v_{geo} are identical to the values of u and v as given above, and the prescribed subsidence is a function of height and the divergence. Chapter 4.2 gives insight into the equations, values and vertical profile of the subsidence.

A.4 Large scale fluxes - ls_flux.inp

The ls_flux inputfile consist of two parts. The first part contains the fluxes of several variables which can be specified for several timesteps, and the second is identical to the lscale.inp input file for every specified timestep in the first part.

The only time dependent variable is the liquid surface temperature (K), which is here specified for every hour, following the course of the nocturnal surface temperature of 16 August 2016 for the SBL simulation and the diurnal $\theta_{l,surf}$ of 17 August 2016 for the CBL simulation. Figure 4.1 in chapter 4.3 given a schematic overview of the temperature courses of both simulations.

A.5 Additional inputfiles

Beside these four inputfiles, the performed simulations also require three other input files. If passive scalars are prescribed DALES, also requires an initial vertical profile of all the specified scalars, which are all 0 at the start of the simulation. The other two inputfiles are the locations of the passive scalars and the locations of the buildings. The specifics of these input files are given in chapter 2.7 and 2.5.2, respectively.

B

Transition of GABLS1 to SBL

The stable boundary layer implemented for this study is based on the SBL simulated by the GABLS1 case. However, as stated in chapter 4.8, there are several important differences between the two simulations. These variables are changed one by one to study the impact of the different modifications on the stability of the boundary layer of the simulation.

Of these alterations, the decrease in wind speed and the hourly decline of the virtual temperature are expected to have the largest impact. In a stable boundary layer at night time, when the surface is no longer heated by the radiation of the sun, the largest remaining factor of turbulence in the shear turbulence, driven by the wind velocity. A smaller wind velocity automatically translates to a smaller shear turbulence. A larger decrease of the surface temperature per hour will probably mean that the (negative) buoyancy will increase. Over all, the impact of all changes are expected to have a dampening effect on all considered variables. First, figure B.1 gives insights into the buoyancy flux of the GABLS1 simulations in comparison with all incremental alteration.

The first three changes (a)domain, b)wind velocity and c)surface temperature) don't seem to impact the buoyancy flux significantly. However, the larger decrease of the hourly surface temperature flux, which as table 4.1 presents, is tripled. This almost directly translates to the buoyancy flux, which also triples. The buoyancy is the upward acceleration of air, mainly caused by temperature differences. Therefore it holds that an increase in the (negative) temperature flux brings an increase in the buoyancy flux. Interesting is the decrease in the buoyancy flux due to a lower wind velocity, whereas this increase can not be directly seen when this is the only changed variable (figure B.1.b.). A smaller wind velocity has a direct impact on the turbulence, where the shear turbulence is mostly based on the size of the wind velocity. This decrease in shear TKE due to a smaller wind velocity, could impact the ratio at which the air at the surface is mixed with the air above. In the simulation with all differences combined, the surface temperature decrease over time is larger, however, its effect on the buoyancy flux is probably restrained by the decrease of shear TKE.

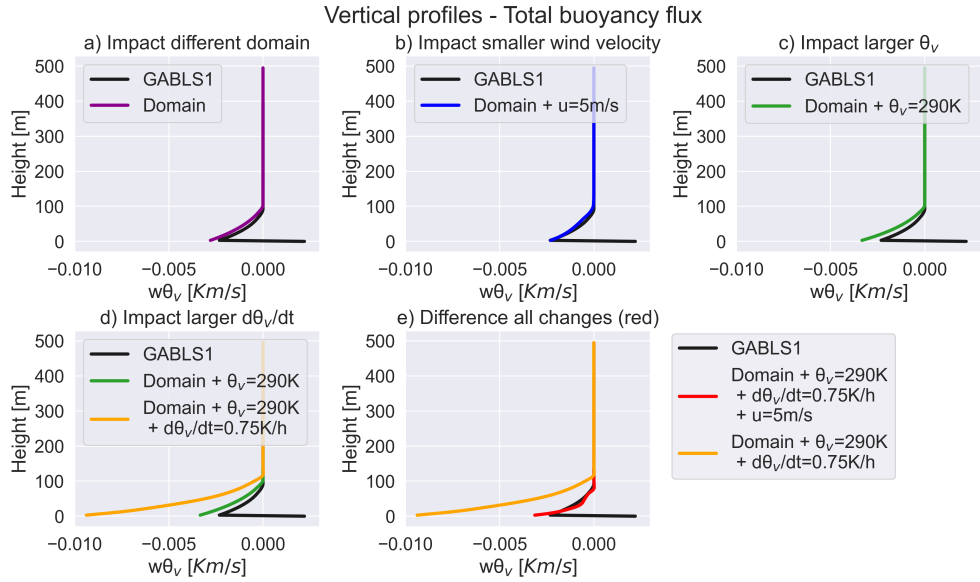


Figure B.1: The vertical profiles of the total buoyancy flux of the GABLS simulation in comparison to small alterations to the desired simulation state, where a) changes the domain size, b) the wind velocity, c) the virtual surface temperature, d) the hourly virtual surface temperature flux and e) gives a comparison of all the changes to the original case study. The alterations in variables are given in the legend of the graph, all unnamed variables are the unchanged variables of the GABLS simulation as displayed in table 4.1.

A similar effect is seen in figure B.2, where the total and the sub-surface TKE remain relatively constant, with a significant increase of the total TKE when $\partial\theta_{v,surf}/\partial t$ increases and a decrease in turbulence when the wind velocity of 8 ms^{-1} is replaced by 5 ms^{-1} . Advantageous is the decreases vertical profile of the SFS-TKE in the desired simulation (in red in figure B.2.e). This means that most of the turbulence is resolved by the model, whereas the other simulations portray a SFS-TKE/Total TKE ratio proximating 0.9. This ratio in the simulated SBL implemented in this study is smaller than 0.4. These are shown in figure B.3.

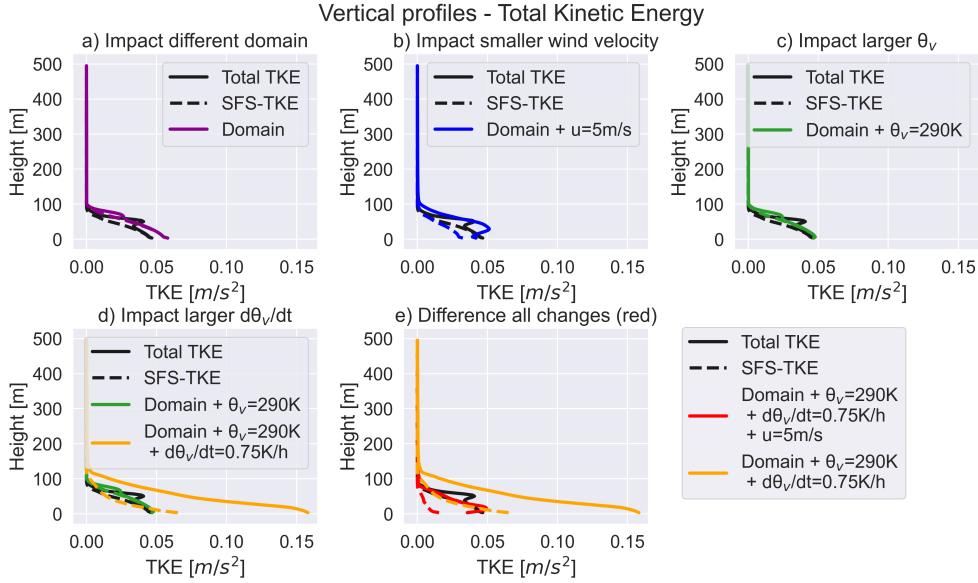


Figure B.2: The vertical profiles of of the total turbulent kinetic energy (TKE) and the sub-filter surface TKE of the GABLS simulation in comparison to small alterations to the desired simulation state, where a) changes the domain size, b) the wind velocity, c) the virtual surface temperature, d) the hourly virtual surface temperature flux and e) gives a comparison of all the changes to the original case study.

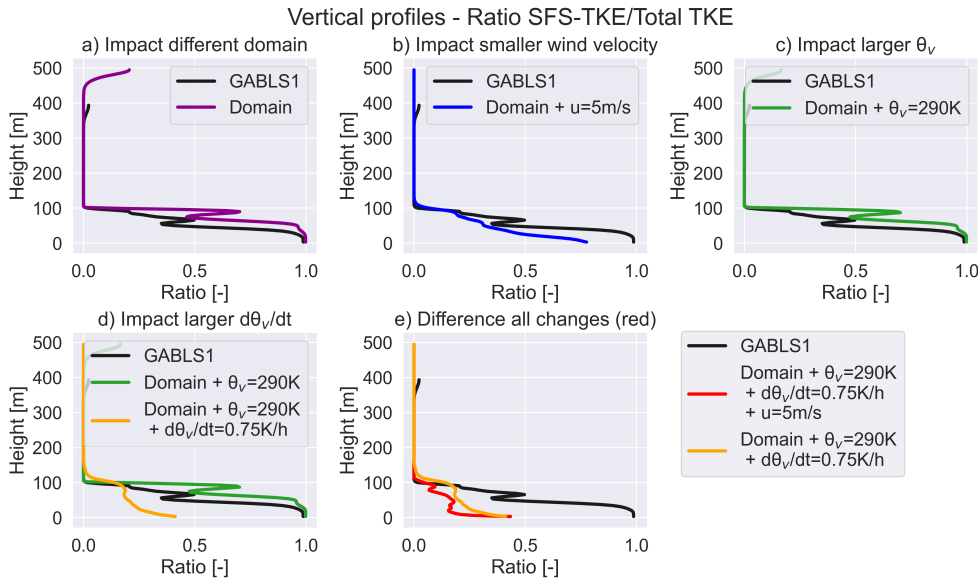
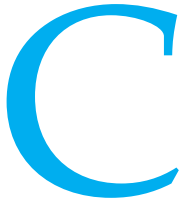


Figure B.3: The vertical profiles of of the ratio of the SFS-TKE to the total turbulent kinetic energy (TKE) of the GABLS simulation in comparison to small alterations to the desired simulation state, where a) changes the domain size, b) the wind velocity, c) the virtual surface temperature, d) the hourly virtual surface temperature flux and e) gives a comparison of all the changes to the original case study.



Results of the Point Sources

The analyses performed for the line source are repeated for the the point sources. Figure C.1 gives the horizontal and vertical distribution of the concentrations of the SBL simulations of first the Gaussian plume model, than the DALES simulation without obstacles, followed by the DALES simulation with obstacles. If an horizontal or vertical distribution is given of one point source, the results of the middle point source are displayed, at $y = 430\text{m}$.

The plumes of the concentrations obtained from the Gaussian plume model are larger than the plumes calculated by DALES, and are larger downwind form the sources. Moreover, they reach higher elevations than the concentrations in the DALES simulations. The reason for these differences in results should be further investigated, as to which model is a more accurate portrayal of a surface point source in a stable boundary layer without obstacles.

As already seen with the result of the line source, the concentrations upwind from the source and around the edges of the plume have negative values in the DALES simulations, due to the applied second order advection scheme. Furthermore, the concentration of the pollutant is significantly more concentrated near the source when buildings are present, then when they are not. However, the plume direction with the presence of buildings is still heavily influenced by the wind direction.

Figure C.2 display the same figures as figure C.1 for the convective boundary layer. As concluded by the line source analyses, the concentrations as obtained from the Gaussian plume model of the CBL are considerably higher than the concentrations as calculated by DALES.

The presence of buildings has a similar effect on the concentrations in the CBL as in the SBL, however less significant: the plume of the concentration of the pollutant is more concentrated at the source. The plume direction is however highly affected by the obstacles in a CBL.

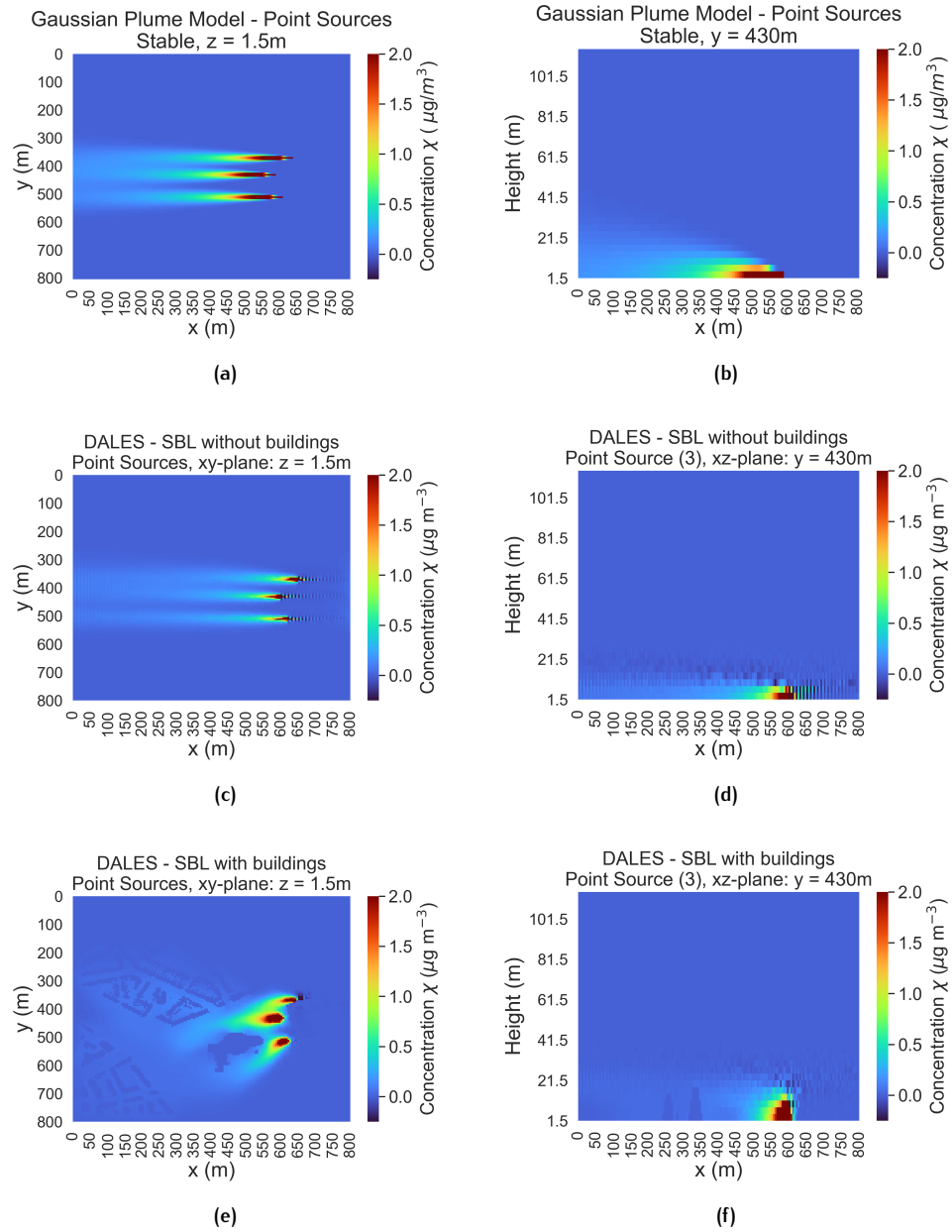


Figure C.1: Vertical and horizontal profiles of the three point sources of time-averaged concentrations of the SBL as obtained from the Gaussian plume model and the DALES simulation, with obstacles and without.

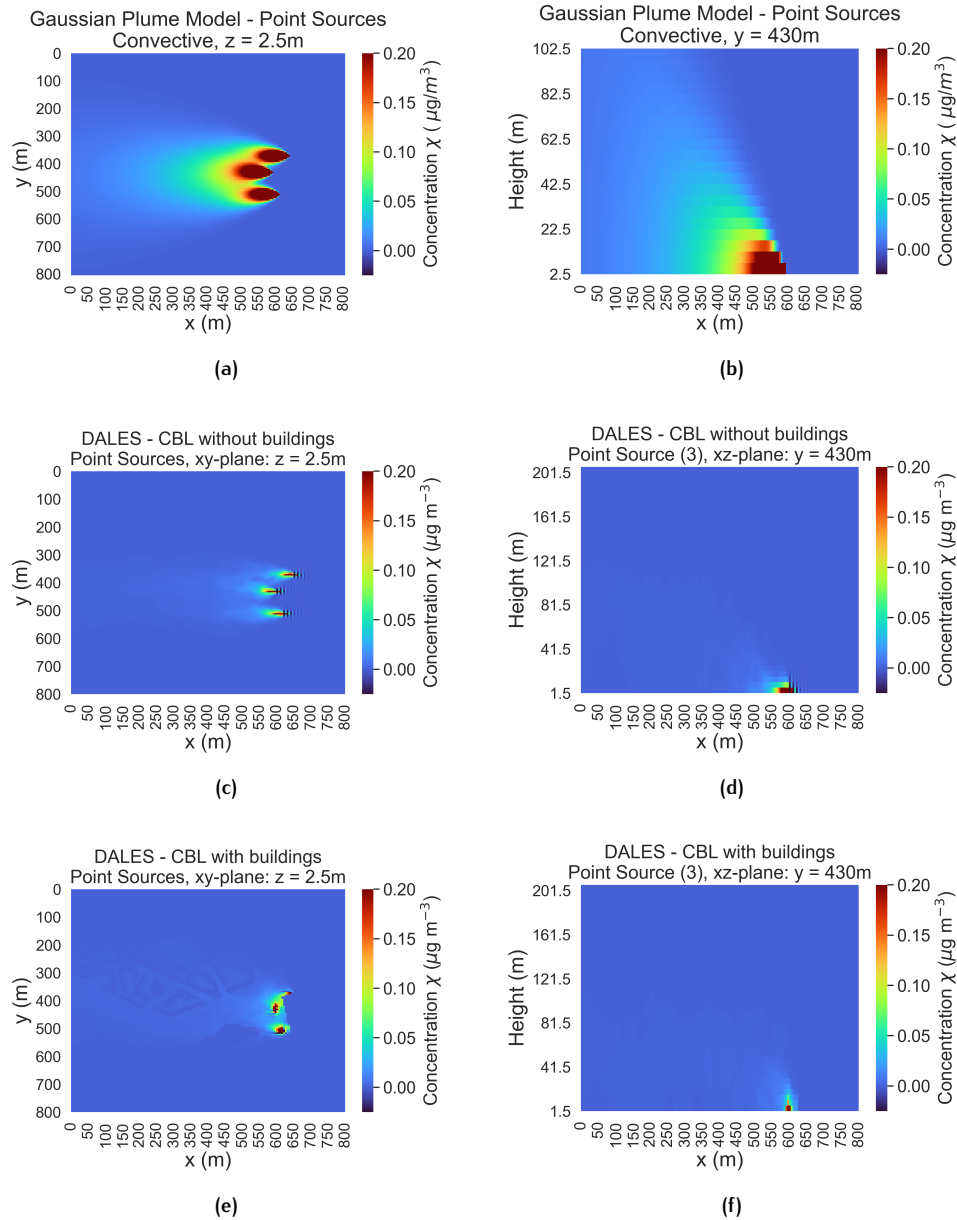


Figure C.2: Vertical and horizontal profiles of the three point sources of time-averaged concentrations of the CBL as calculated by the Gaussian plume model and the DALES simulation, with obstacles and without.

Figure C.3 gives the surface concentrations of both the SBL and CBL simulations as obtained from DALES, comparing the concentrations with and without obstacles. As stated before, the concentrations of the simulations with buildings are highly concentrated at the source, regardless of the stability of the atmosphere.

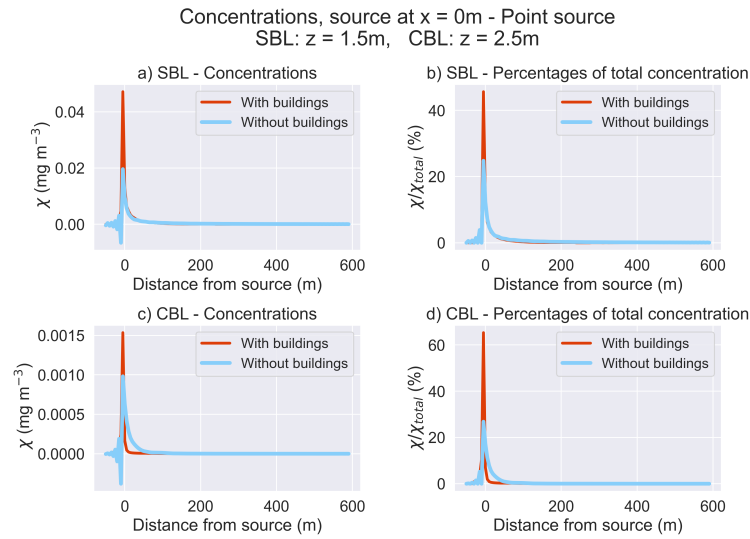


Figure C.3: The time-averaged point source concentrations χ in the downwind direction and the percentages of the total concentration. The red lines represent the results of the simulation with buildings and the blue without. a) and b) give the concentration and the percentages of the SBL simulations, and c) and d) of the CBL simulations.

Figure C.4 gives the vertical profiles of the pollutants concentrations several distances from the source of the SBL and CBL simulations with and without buildings. The presence of buildings increases concentrations at higher levels in the atmosphere, and the concentrations are more concentrated around the source.

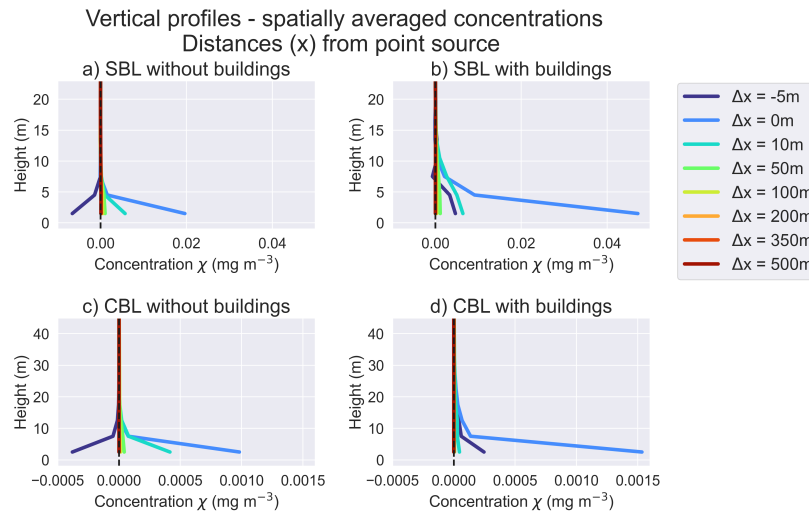


Figure C.4: The time-averaged, spatially averaged, vertical profiles of the concentration at several downwind distances from one of the point sources. a) and b) give the concentration and the percentages of the SBL simulations, and c) and d) of the CBL simulations.

Colophon

This document was typeset using L^AT_EX. The document layout was generated using the `arsclassica` package by Lorenzo Pantieri, which is an adaption of the original `classithesis` package from André Miede.

